Thermal Tides in the Atmosphere of Venus: Comparison of Model Results with Observations[1]

JUDITH BURT PECHMANN[2] AND ANDREW P. INGERSOLL

Division of Geological and Planetary Sciences, California Institute of Technology, Pasadena, CA 91125

(Manuscript received 15 May 1984, in final form 27 August 1984)

ABSTRACT

A linearized primitive equation (LPE) model is developed to study thermal tides in the atmosphere of Venus. The LPE model describes diurnal and semidiurnal oscillations of a cyclostrophically balanced atmosphere in which zonal velocity varies with altitude and latitude. The numerical algorithm follows Staniforth and Daley. The solar thermal forcing is increased algebraically in time to separate the forced tidal response from free atmospheric oscillations. Parameters of the basic state and forcing agree with *Pioneer Venus* observations. Results of the model are compared with the solar-fixed component of brightness temperature variations measured by Taylor *et al.* and Elson using data from the *Pioneer Venus* orbiter infrared radiometer (OIR). The comparison is made by convolving the computed model radiances with the weighting functions of the OIR channels. Agreement between LPE model results and OIR observations is excellent. Two interesting features of the OIR data are accounted for, namely, the slow variation of phase with altitude and the dominance of the semidiurnal oscillation over the diurnal oscillation. Success of the LPE model opens the way for calculating tidal transports of heat and momentum and assessing the role of tides in maintaining the Venus super-rotation.

1. Introduction

Atmospheric thermal tides are planetary-scale waves forced by the variation in the absorption of solar radiation from day to night. On Venus, data on the tides come from infrared remote sensing of temperatures at the cloud tops and above. Earth-based observations of thermal emission from the clouds indicate a semidiurnal brightness temperature oscillation larger than the diurnal oscillation (Diner *et al.*, 1982). The semidiurnal maxima occur a few hours before both noon and midnight. The *Pioneer Venus* orbiter infrared radiometer (OIR) confirms the ground-based observations and provides information on the vertical structure of the tidal oscillation up to the altitudes of 100 km (Taylor *et al.*, 1980; Elson, 1983; Schofield and Taylor, 1983; Taylor *et al.*, 1983). At most altitudes the semidiurnal tide is larger than the diurnal tide, and the phase of the semidiurnal tide varies slowly with height.

Two features in particular of these observations need to be explained. First, if the slow phase variation of the semidiurnal tide is due to either trapping or damping, the maxima should occur after noon and after midnight, lagging the maxima in semidiurnal forcing at noon and midnight. Second, since the amplitude of the diurnal forcing is twice as great as that of the semidiurnal forcing, the diurnal tidal response should be greater than the semidiurnal response. This paper will provide an explanation of these two problems.

As a first step, we model the tides numerically, that is, without the approximations of classical tidal theory. We then simulate the observations by convolving our solution with the OIR weighting functions. The computed brightness temperatures agree with observations within acceptable limits. The success of the numerical model increases confidence in our knowledge of the mean state of the Venus atmosphere and provides us with the opportunity to determine the importance of energy and angular momentum transport by the tides.

The amplitude and phase of the semidiurnal pressure oscillation at the surface is of special interest on Venus because it determines the solar gravitational torque on the atmosphere. The torque may act to accelerate the atmospheric rotation and/or maintain the rotation of the planet (Gold and Soter, 1969, 1971, 1979; Ingersoll and Dobrovolskis, 1978; Dobrovolskis and Ingersoll, 1980; hereafter, the latter two papers will be referred to as DI). Our results are consistent with DI in finding that the surface pressure oscillation generated by the heating in the clouds is negligible compared to that generated by heating at the ground, even though the cloud-level heating is

[1] Contribution No. 4069 from the Division of Geological and Planetary Sciences, California Institute of Technology, Pasadena, CA 91125.

[2] Present affiliation: Department of Meteorology, University of Utah, Salt Lake City, UT 84112.

about 30 times greater. The opposite is true on Earth and Mars where forcing at high altitudes enhances the semidiurnal surface pressure response. As pointed out by DI, this enhancement does not occur on Venus because of the difference in diurnal period between the upper and lower atmosphere. We have not been able to determine accurately the magnitude of the torque on the atmosphere because the model is ill-constrained near the ground.

To solve for Venus thermal tides we have developed a linearized primitive equation (LPE) model based on the nonlinear general circulation model of Staniforth and Daley (1977). They supplied us with a computer code of their model, which we modified extensively. Classical tidal theory is not applicable on Venus because it requires the assumption of uniform rotation with height in order to obtain equations separable in height and latitude. On Venus the solar day is 117 earth days at the ground and about 4 earth days at 65 km; thus, the variation in rotation rate cannot be ignored. In the LPE model the latitudinal and vertical structures are coupled through terms involving the shear in the mean zonal wind. The LPE model retains the spherical geometry of the nonlinear model, which is appropriate for global-scale waves such as tides.

We obtained results in agreement with the OIR tidal amplitudes and phases using, as input to the LPE model, parameters which are in the range allowed by available data. The input parameters are the mean zonal wind and tidal forcing (solar heating) as functions of height and latitude, and the global mean static stability and coefficients of Newtonian cooling and Rayleigh friction as functions of height. The variation in the static stability with latitude is determined from the assumption of cyclostrophic balance. We will refer to the mean zonal wind, static stability and the coefficients of Newtonian cooling and Rayleigh friction as the basic state of the Venus atmosphere.

In this paper we outline the LPE model in Section 2. In Section 3 we discuss the data available on the basic state of the Venus atmosphere and the range in basic states explored by the model calculations. The results of the calculations along with an explanation of the OIR tidal data are presented in Section 4. Finally, in Section 5 we discuss the sensitivity of the model results to changes in the basic state and in the OIR weighting functions.

In a future paper we will present the energy and angular momentum fluxes due to the tides. We will compare the angular momentum flux to estimates of torque due to eddy viscosity and the energy flux to the radiative imbalance at each latitude. We will also estimate the angular momentum fluxes due to the mean meridional circulation forced by the combined effects of the radiative imbalance and the tidal energy transport.

2. The linearized primitive equation model

A full description of the LPE model is given in Pechmann (1983). Following Staniforth and Daley (1977, hereafter referred to as SD), we examine the primitive equations. The vertical coordinate is $\sigma = p/p_s$, where p is pressure and p_s is surface pressure. The equations are

$$\zeta_t + \zeta/\tau_R = G, \tag{1}$$

$$\sigma W_{\sigma\sigma t} + \sigma(W_\sigma/\tau_R)_\sigma + R\nabla^2(T - \sigma T^*_\sigma q) = \sigma H_\sigma, \tag{2}$$

$$T_t - \sigma T^*_\sigma q_t + (T - \sigma T^*_\sigma q)/\tau_N - \gamma^* W = J, \tag{3}$$

$$q_t - W^s = K, \tag{4}$$

where G, H, J and K are defined for the nonlinear case by SD. The prognostic variables are the vorticity ζ, the variable $W = -\int_0^\sigma D d\sigma$ where D is the horizontal divergence, the temperature T and $q = \ln p_s$. In addition, we define $W^s = -\int_0^1 D d\sigma$. A subscript indicates differentiation with respect to that variable. In (1)–(4) t is time, R the gas constant, $T^*(\sigma)$ the global mean temperature and $\gamma^*(\sigma) = RT^*/C_p\sigma - dT^*/d\sigma$ the global mean static stability. The specific heat at constant pressure is C_p, and τ_R and τ_N are time constants for Rayleigh friction and Newtonian cooling, respectively. Equations (1) and (2) are the equations of motion, (3) is the thermodynamic equation and (4) is the continuity equation. The divergence equation (2) has been differentiated with respect to σ, and the hydrostatic relation $\sigma\Phi_\sigma = -RT$ has been used to eliminate Φ.

The boundary conditions are $\dot\sigma = 0$ at $\sigma = 0$ and at $\sigma = 1$, where $\dot\sigma$ is the vertical velocity in σ coordinates. These conditions have been used to obtain a vertically integrated form of the continuity equation and a diagnostic expression for $\dot\sigma$:

$$\dot\sigma = (\sigma - 1)(\hat D + \hat{\mathbf{V}}\cdot\nabla q) + \hat D^\sigma + \hat{\mathbf{V}}^\sigma\cdot\nabla q, \tag{5}$$

where for any function F,

$$\hat F^\sigma = \int_\sigma^1 F d\sigma; \quad \hat F = \int_0^1 F d\sigma.$$

Our model includes dissipation in the form of Rayleigh friction and Newtonian cooling. The dissipation terms are used to form a "sponge layer" in the upper atmosphere, which absorbs upward propagating energy. The sponge layer is necessary because without it the boundary condition $\dot\sigma = 0$ at $\sigma = 0$ causes spurious reflections of upward propagating waves. In fact, due to the vertical discretization, the effect of the boundary condition at $\sigma = 0$ is the same as that of a rigid-lid at a finite height (Lindzen *et al.*, 1968; Kirkwood and Derome, 1977). The vertical profiles of τ_R and τ_N are discussed in Section 3.

To linearize, we express all dependent variables as a sum of a basic state component plus a perturbation. For example,

$$T(\sigma, \lambda, \phi, t) = T^*(\sigma) + T_1(\sigma, \lambda) + T'(\sigma, \lambda, \phi, t),$$

where λ is latitude and ϕ is longitude. To be consistent with SD we have broken up our basic state temperature into a global mean profile $T^*(\sigma)$ and a latitudinally varying component $T_1(\sigma, \lambda)$. In general, a superscript asterisk denotes a global mean basic state quantity, and a prime denotes the unknown perturbation.

The zonal wind is $u = r\Omega(\sigma, \lambda)\cos\lambda + u'(\sigma, \lambda, \phi, t)$, where Ω is the basic state rotation and r the radius of the planet. The basic state meridional wind v^* is zero, so $v = v'(\sigma, \lambda, \phi, t)$. It follows that $D^* = W^* = 0$ and $\zeta^* = -(1/\cos\lambda)(\partial/\partial\lambda)(\cos^2\lambda\Omega)$. In general, $q^* = (\ln p_s)^*$ may depend on λ; this dependence represents zonally averaged topography. For the results reported here, we have set $q^* =$ constant. The above basic state expressions and (5) imply that $\dot{\sigma}^* = 0$.

The linearized equations are obtained by substituting expressions for the basic state plus perturbation quantities into (1)–(4) and keeping only terms that are of first order in the perturbations. The terms on the left-hand side of (1)–(4) are already linear, so the main work comes in finding G', H', J' and K'. We obtain

$$G' = -\Omega\frac{\partial\zeta'}{\partial\phi} - (\zeta^* + f)D' - \frac{v'}{r}\frac{\partial}{\partial\lambda}(\zeta^* + f) + \frac{R}{r^2}\frac{\partial T_1}{\partial\lambda}\frac{1}{\cos\lambda}\frac{\partial q'}{\partial\phi} - \frac{R}{r^2\cos\lambda}\frac{\partial T'}{\partial\phi}\frac{\partial q^*}{\partial\lambda} + \frac{1}{\cos\lambda}\frac{\partial}{\partial\lambda}\left(\cos^2\lambda\dot{\sigma}'\frac{\partial\Omega}{\partial\sigma}\right),$$

$$H' = -(\zeta^* + f)\zeta' + \frac{u'}{r}\frac{\partial}{\partial\lambda}(\zeta^* + f) + \frac{1}{\cos\lambda}\frac{\partial}{\partial\lambda}(\zeta'\cos^2\lambda\Omega) + RT_1\nabla^2 q' + \frac{R}{r^2}\frac{\partial T_1}{\partial\lambda}\frac{\partial q'}{\partial\lambda}$$
$$+ \frac{\partial\Omega}{\partial\sigma}\frac{\partial\dot{\sigma}'}{\partial\phi} + \nabla^2(u'r\cos\lambda\Omega) + \frac{1}{r^2\cos\lambda}\frac{\partial}{\partial\lambda}(RT'\cos\lambda\partial q^*/\partial\lambda),$$

$$J' = \sigma\hat{\Omega}T^*_\sigma\frac{\partial q'}{\partial\phi} + \sigma T^*_\sigma\frac{\hat{v}'}{r}\frac{\partial q^*}{\partial\lambda} - \frac{v'}{r}\frac{\partial T_1}{\partial\lambda} - \Omega\frac{\partial T'}{\partial\phi} + \dot{\sigma}'(\gamma^* + \gamma_1) - (W' - \sigma W^{s'})\gamma^*$$
$$- \frac{RT_1}{C_p}\hat{D}' + \frac{R(T^* + T_1)}{C_p}(\Omega - \hat{\Omega})\frac{\partial q'}{\partial\phi} + \frac{R(T^* + T_1)}{C_p}\frac{(v' - \hat{v}')}{r}\frac{\partial q^*}{\partial\lambda} + \frac{Q'}{C_p},$$

$$K' = -\hat{\Omega}\frac{\partial q'}{\partial\phi} + \frac{\hat{v}'}{r}\frac{\partial q^*}{\partial\lambda}.$$

Here Q' is the tidal forcing. For the tides, $\partial/\partial\phi$ becomes im, where m is an integer. The Coriolis parameter f depends on the choice of reference frame, and will be specified below.

Our numerical algorithms for integrating (1)–(4) in time and space follows SD exactly. Details are given in SD and in Pechmann (1983). The model of SD is discretized using finite elements in the vertical dimension and spherical harmonics in the horizontal. To increase the efficiency of the calculation, the interaction terms between basic state and perturbation are evaluated on a Gaussian grid in $\sin\lambda$. The spherical harmonic components of the interaction terms are then determined numerically. No aliasing results from this procedure as long as a sufficient number of Gaussian grid points are used. The time discretization is semi-implicit, which means that certain terms are evaluated implicitly, i.e., as a mean of their values at the past and future time steps. The terms evaluated implicitly are those controlling the propagation of gravity waves. This discretization has the effect of stabilizing the model with respect to short period gravity waves, allowing a longer time step to be taken (Robert *et al.*, 1972).

To extract the forced tidal fields from our time-stepping model, a convergence scheme is required that will arrive at the forced solution from arbitrary initial conditions. Our first step is to use a solar-fixed reference frame, i.e., one in which the line from the center of the sun to the center of Venus is fixed. In this reference frame, the tidal solution has no time dependence, while the free modes excited by the initial conditions either oscillate with a finite frequency or grow slowly, as discussed below. The free oscillatory part of the solution is separated from the forced steady part by increasing the forcing algebraically in time. The forced response increases in proportion to the forcing. Since the free modes are only present due to excitation by the initial conditions, they are unaffected by the forcing, and their amplitudes remain constant. We have found that a quadratic rate of increase in the forcing converges to the forced solution, although any power of time is allowable. Of course, a free oscillation mode with the tidal frequency might exist. Then we would be forcing at a resonance, and very large tidal amplitude would result. We have found no evidence of a resonance in our solutions.

We can illustrate how this method works in a simple system. Consider the equation

$$\frac{du}{dt} + i\omega u = F,$$

where F is a constant forcing, ω a constant frequency and u is unknown. The forced, or particular, solution is $u_p = F/i\omega$. There is only one free, or homogeneous, mode in the system: $u_H = Ae^{-i\omega t}$, where A is a free parameter. If we arbitrarily apply the initial condition $u = 0$ at $t = 0$, then

$$u(t) = \frac{F}{i\omega}(1 - e^{-i\omega t}),$$

which will never converge to $F/i\omega$. Now consider the equation

$$\frac{dv}{dt} + i\omega v = Ft^2.$$

The particular solution is $v_p = (F/i\omega)(t^2 - 2t/i\omega - 2/\omega^2)$, while $v_H = Ae^{-i\omega t}$. With the initial condition $v = 0$ at $t = 0$, we obtain

$$v = (F/i\omega)\left[t^2 - \frac{2}{i\omega}t - \frac{2}{\omega^2}(1 - e^{-i\omega t})\right].$$

As t approaches ∞, v/t^2 approaches $F/i\omega$, the desired forced solution.

We tested the validity of our model by computing the tidal fields in the earth's atmosphere and comparing our results to the solution from classical tidal theory. In the classical theory the basic state zonal flow of the atmosphere with respect to the solid planet is set equal to zero. Also, internal dissipation and topography are ignored. The other basic state variables are functions of height only.

Setting the basic state zonal flow equal to zero relative to the surface is equivalent to setting u^*, the basic state zonal velocity, equal to $r\Omega_d \cos\lambda$, where $\Omega_d = 2\pi/P_d$ and P_d is the length of a solar day. The terms in our model involving Ω_d are then identical to those involving $f_d = 2\Omega_d \sin\lambda$, the Coriolis parameter in a rotating frame. Since our frame still rotates with the motion of the planet around the sun, there is also a Coriolis term $f_y = 2\Omega_y \sin\lambda$, where $\Omega_y = 2\pi/P_y$, and P_y is the length of the year. For a rapidly rotating planet like Earth, f_y may be neglected. We will retain f_y when modeling Venus tides, and we choose the direction of rotation such that $\Omega > -\Omega_y > 0$. Thus, in the expressions for G' and H', we set $f = f_y < 0$.

We have modeled the earth's diurnal thermal tide using the same basic state and forcing functions as Lindzen (1967), so that our results may be compared to those he obtained using classical theory. The atmosphere is isothermal with $T^* = 260$ K. Other nonzero basic state quantities required are the static stability $\gamma^* = RT^*/C_p\sigma - dT^*/d\sigma$, and $\zeta^* = 2\Omega_d \sin\lambda$. The sponge layer is produced by setting $\tau_R = \tau_N = \tau_0\sigma$, where $\tau_0 = 1.2 \times 10^7$ years. In the lower atmosphere this dissipation is negligible. The altitude and latitude dependence of the forcing is given in Lindzen (1971). The numerical model parameters were chosen to provide adequate resolution and convergence. Figure 1 shows our results for the diurnal perturbation in v' compared with Lindzen's (1967) calculation. The diurnal tide shows a great deal of vertical and horizontal structure, all of which is reproduced by our model. Similar excellent agreement is obtained at other latitudes and in other tidal components.

The semidiurnal tide is more sensitive to the temperature profile, so Chapman and Lindzen (1970)

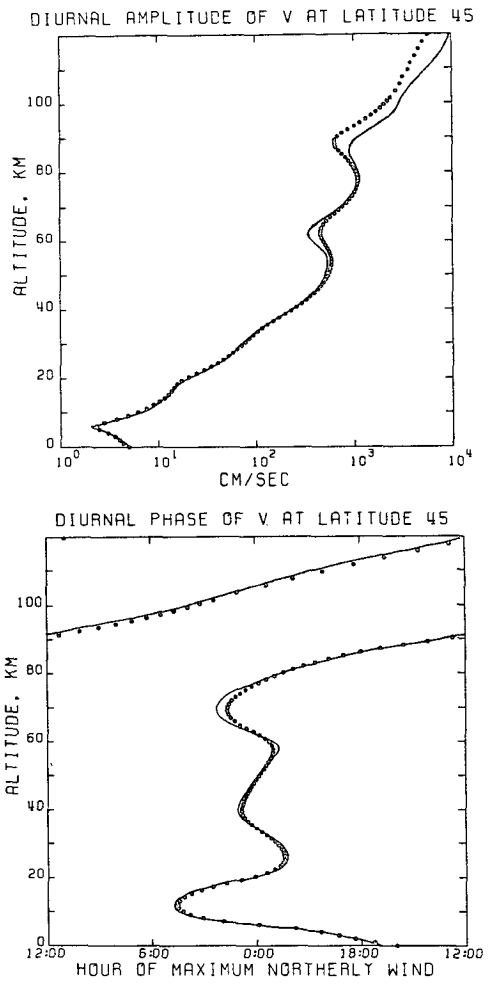

FIG. 1. Comparison of results from the LPE model (dots) and classical tidal theory (curve). The top panel shows the amplitude and the bottom panel the phase of the diurnal oscillation of the north–south velocity v' at a latitude of 45°. The input parameters and the smooth curve are from Lindzen (1967, 1971) for the terrestrial thermal tide.

use a more realistic profile than the isothermal one. Below 100 km the profile used in the LPE model coincides with the standard equatorial profile used in Chapman and Lindzen (1970) for calculating the semidiurnal tide. The forcing functions are the same as those used in the diurnal case, with the amplitude adjusted appropriately. The sponge layer was the same as that used for the diurnal case. Our results for the semidiurnal tide in v' are shown in Fig. 2. Once again, our model agrees closely with the classical theory.

An important characteristic of a dynamical model like ours is its performance in conserving energy. The LPE model conserves energy in the sense that the space discretization introduces no spurious terms in the global energy balance. Perturbation energy is gained from the forcing and is lost by dissipation. Perturbation energy is also gained from, or lost to, the basic state through interactions involving $\partial\Omega/\partial\sigma$ and $T_1(\sigma, \lambda)$. This conversion does not violate the assumption that the basic state terms, which are zero-order in the perturbation, are constant in time because the perturbation energy is a second-order quantity.

A spurious growth of energy may occur in the LPE model because of explicit terms in the time discretization. Physical instabilities may also be present when $\partial\Omega/\partial\sigma \neq 0$, and would cause an exponential growth of perturbation energy. Since we are looking for a stable, forced solution, these instabilities are also undesirable.

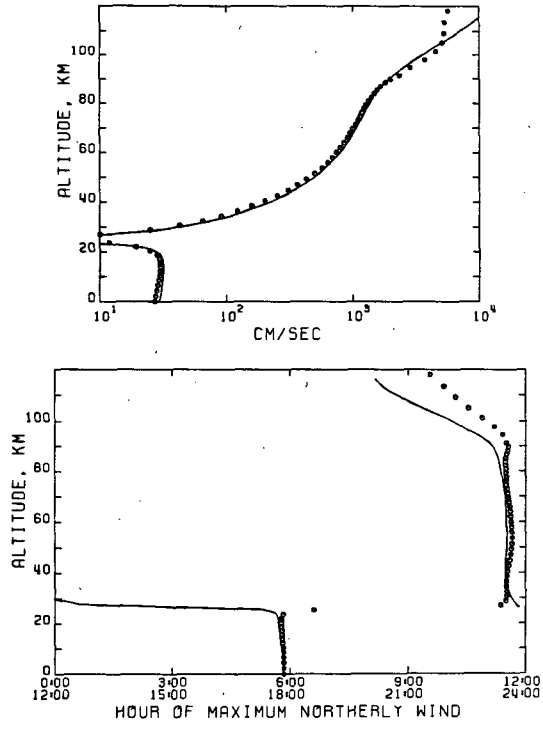

FIG. 2. As in Fig. 1 except that the semidiurnal amplitude (top) and phase (bottom) are given at a latitude of 30°. The input parameters are from Chapman and Lindzen (1970) and Lindzen (1971).

Unfortunately, there is an instability in the LPE model for Venus thermal tides. However, the growth rate is slow enough for the model to be nearly converged before the instability becomes important. The instability seems to be generated in the low static stability region near the ground. We do not know whether this instability is of physical or numerical origin, but it is possible that it is related to shear instability. At the equator the Richardson number Ri is less than 1.0 in the lowest two scale heights and is less than 0.25 in a narrow layer near the top of the second scale height. At these heights the static stability decreases with increasing latitude, so Ri will decrease toward the pole. The condition $\mathrm{Ri} < 0.25$ is generally sufficient for instability. The instability criterion was not satisfied in the LPE model for terrestrial tides or in any case where $\partial\Omega/\partial\sigma = 0$. In these cases, the production of perturbation energy by solar forcing is balanced by dissipation in the sponge layer. Determining the exact nature of the instability for Venus is a top priority in future work with the LPE model.

As the final topic in this section, we discuss the "gravity wave equivalent" model for the tides. Since the LPE model is expensive to run, it is convenient to have a simpler model with which to explore the parameter space allowed by data on the Venus basic state. Many characteristics of the tides can be investigated using a simple gravity wave system.

The gravity wave system we use is two-dimensional in space. The dependence of the perturbations on the horizontal coordinate x is assumed to be e^{ikx}, where k is constant. We seek the tidal response as a function of σ. To represent tides in this two-dimensional system, we identify x with the zonal direction so that the e^{ikx} dependence corresponds to $e^{im\Phi}$ in the tides, where m is the zonal wavenumber. The latitude dependence of the tides is ignored except in terms involving the horizontal Laplacian operator. The equation for the vertical structure of the gravity waves and that for the vertical structure of the tides in classical tidal theory are exactly the same if, in the gravity wave system, we define

$$\nabla^2 T' = -k^2(\epsilon/4)T',$$

where T' is the temperature perturbation and ϵ is an eigenvalue of Laplace's latitudinal tidal operator. For each positive or negative ϵ there is a latitudinal tidal mode, called a Hough function, with an associated vertical structure. The gravity wave model may be used to obtain the tidal vertical structure if ϵ is known. The total tidal solution is obtained by summing over the Hough modes.

When the basic zonal velocity u^* depends on height, strictly speaking, ϵ does not exist. However, to investigate Venus tides with the gravity wave model we define an ϵ that depends on height. Lindzen

(1970) gives a value of ϵ for the lowest diurnal and semidiurnal Hough modes for the Venus solid body rotation rate. For the diurnal mode $\epsilon = 2.13$ and for the semidiurnal $\epsilon = 2.04$. We use these values at the ground, assuming the mean zonal wind is zero there. As Ω increases, ϵ approaches a constant. At the cloud tops the atmosphere rotates with a maximum Ω of about 2π/(4 days), which is rapid enough so that the rapid rotation values of ϵ should be valid. These are $\epsilon = 127.53$ and $\epsilon = 11.16$ for the diurnal and semidiurnal tides, respectively, for the lowest order Hough mode. To determine ϵ for values of u^* intermediate between the ground and the cloud tops, we assume a linear dependence of ϵ on u^*.

The only way to test this method is to compare results from the gravity wave model with the full LPE model results. We have found that the gravity wave model results reproduce the general features of the LPE model solution at low latitudes. The gravity wave solution is not valid at high latitudes because it approximates the vertical structure of the lowest Hough mode, which has a low amplitude in the polar region.

3. Venus basic state and tidal forcing

Our nominal basic state and forcing functions are consistent with available basic state data and optimize the model fit to the OIR tidal data. The nominal basic state and forcing functions are not unique, however, due to uncertainties both in the basic state and forcing function data and in the tidal data. These uncertainties allow the possibility of trade-offs in adjusting the various basic state parameters. Other basic states and forcing functions, either similar to or significantly different from the nominal case, that provide as good a fit to the OIR data may exist. However, it is not feasible to search the entire allowed parameter space. The *existence* of the nominal case that is consistent with all available data is the point of most significance for this paper.

The static stability of the atmosphere is an important parameter in determining the vertical structure of thermal tides. The LPE model requires as input the global average stability in the form

$$\Gamma = \Gamma_a + dT^*/dz,$$

where Γ_a is the adiabatic lapse rate and z is height in kilometers. We base Γ on temperature profiles from several *Pioneer Venus* experiments.

From 14 km up to 56 km the stability profile is based on measurements made by the atmospheric structure experiment on *Pioneer Venus* (Seiff *et al.*, 1980). In this experiment simultaneous measurements were made of temperature and pressure as each probe descended. The temperature sensors on all the probes failed at about 13 km, so the stability below that level could not be determined. The probe data are shown in Fig. 3 along with the basic state for several models. From 35 to 56 km model A (the nominal model) is the average of the four probe profiles, except at 54 km where the average is -0.3 K km^{-1}. Negative Γ causes instability in the model, so at 54 km we set $\Gamma = 0.1$ K km^{-1}. Below about 18 km the probe data show a stable trend. Since theoretical models of the radiative and dynamical state of the deep atmosphere predict an adiabatic profile (Pollack *et al.*, 1980; Stone, 1974), the presence of a stable layer is difficult to explain. For the LPE model we have used a low value of the stability, $\Gamma = 0.05$ K km^{-1}, below 30 km. This value is also more convenient, since low stability makes the model converge faster. The sensitivity of the solution to the value of Γ was investigated using the gravity wave model. The sensitivity of the solution in the upper atmosphere to Γ near the ground is small.

The choice of the static stability profile from 56 to 100 km is of critical importance because the OIR measurements of the tides were made in this region. One source of data is the OIR retrieved temperature profiles. The radiance and weighting functions for each OIR channel and a model for the effect of clouds were used by the OIR team in a deconvolution program to retrieve a temperature profile. In Fig. 3 the shaded region from 65 to 110 km shows the

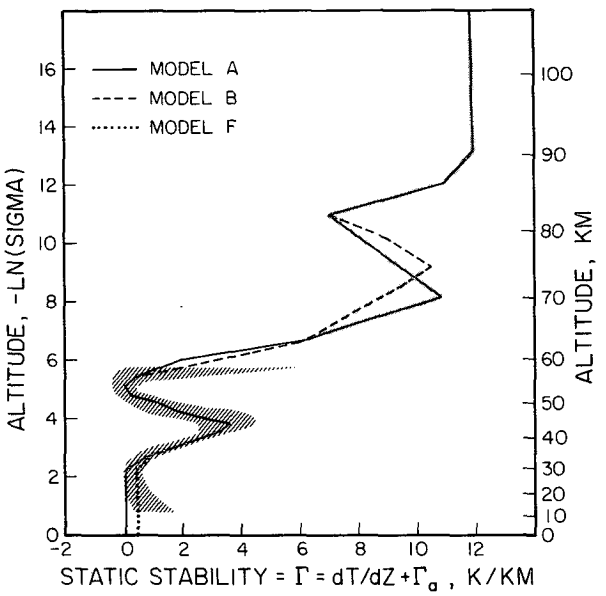

FIG. 3. Profiles of the static stability Γ as measured by *Pioneer Venus* instruments compared to models used in this study. The hatched region below 60 km shows the envelope of instrumental data from the four probes (Seiff *et al.*, 1980). The shaded region shows the envelope inferred from the OIR data (Taylor *et al.*, 1980; Schofield and Taylor, 1983). The width of the envelope indicates the extent to which the profiles measured at different latitudes differ from each other. The solid curve is model A (the nominal model). The dashed curve is model B, and the dotted curve is model F.

envelope of $\Gamma(z)$ profiles at various latitudes derived from the OIR data (Schofield and Taylor, 1983). Model A was chosen to be qualitatively consistent with the OIR profiles in this region. Model A is also qualitatively consistent with the static stability derived from the temperature profiles of the atmospheric structure experiment obtained from deceleration and trajectory information above approximately 65 km (Seiff *et al.*, 1980; see Pechmann, 1983 for details). However, the region of high static stability in the model A profile between 65 and 75 km is broader and less intense than the temperature inversion region observed in most of the radio occultation profiles (Kliore and Patel, 1980).

The basic state temperature profile $T^*(\sigma)$ is derived by writing Γ in the form

$$\Gamma(\sigma) = g/C_p - (g/RT^*)dT^*/d\ln\sigma,$$

using $\Gamma_a = g/C_p$ and $\partial\sigma/\partial z = -\sigma g/RT^*$, the hydrostatic relation. This equation is solved for T^*, using an iteration scheme to obtain a consistent specific heat profile $C_p(\sigma, T)$ (Pechmann, 1983). Finally, γ^* is defined from Γ by

$$\gamma^* = RT^*\Gamma/g\sigma.$$

The vertical profile of the mean zonal wind is the other major factor that determines the structure of thermal tides. Our basic state zonal wind profile from the ground up to 60 km is based on the results of the *Pioneer Venus* differential long baseline interferometry (DLBI) experiment (Counselman *et al.*, 1980). The envelope of DLBI profiles for the four probes are shown in Fig. 4. Also shown is the nominal basic state profile of u^* (model A). The profiles for the day and night probes are almost identical (Counselman *et al.*, 1980). These probes entered at about the same latitude, 30°S, but were separated by 100° in longitude. The similarity in the probe data is evidence for a lack of major longitudinal variations in the zonal wind below 60 km. The sounder probe profile is similar in shape to the day and night profiles, but has higher velocities. The difference in velocity is nearly consistent with a state of solid body rotation at each height between 4°N and 30°S. The velocities measured at the north probe location and at 60°N are higher at most altitudes than predicted by solid body rotation. In our model the basic state is in solid body rotation. Below 60 km it is based on the day, night and sounder measurements. This assumption may have some effect on the validity of our solution in the polar region.

Wind velocity profiles obtained by Doppler tracking of *Venera 8, 9, 10* and *12* are compared to the *Pioneer Venus* DLBI profiles by Schubert *et al.* (1980). The *Venera* profiles show a much larger degree of variability and may indicate spatial or temporal changes in the zonal wind.

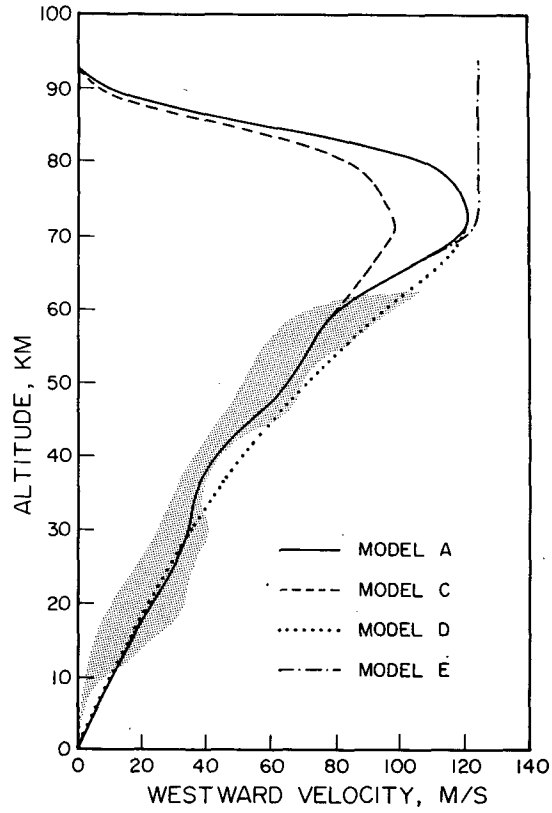

FIG. 4. Profile of the mean zonal velocity (positive westward) measured by the four probes (Counselman *et al.*, 1980) compared to the models used in this study. The shaded region shows the envelope of the observed profiles at latitudes of 4.0, 60.2, −31.3 and −27.4°. The curves show the model profiles at the equator: model A (the nominal model, solid), model C (dashed), model D (dotted), model E (dot-dash).

Above 60 km there are no *in situ* measurements of wind velocity in the Venus atmosphere. However, there is considerable evidence for equatorial winds on the order of 100 m s^{-1} at the cloud top level of about 65 km. Measurements taken by tracking small-scale cloud features in *Pioneer Venus* and *Mariner 10* ultraviolet images (Rossow *et al.*, 1980; Limaye and Suomi, 1981) give equatorial winds of about 95 m s^{-1}. During the *Pioneer Venus* primary mission, the atmosphere at the cloud tops was nearly in solid body rotation from 60°S to 40°N, but at the time of the *Mariner 10* encounter there was a prominent midlatitude jet in each hemisphere. Images taken during the *Pioneer Venus* extended mission indicate that jets (deviations from solid body rotation) of varying strengths appear and disappear with a time scale of several months and may be present in both, either or neither hemisphere (Rossow and Kinsella, 1982). It is unclear which situation is more typical of the circulation. Since the OIR tidal results were obtained during the primary mission, the assumption of solid body rotation in our model should be valid at low to midlatitudes. Ground-based observations

made by measuring Doppler shifts of spectral lines (Traub and Carleton, 1975) and by heterodyne techniques (Betz *et al.*, 1976, 1977) support the existence of high retrograde zonal winds at the cloud tops.

It has not been determined how far above the cloud tops the rapid winds extend or what peak value is reached. Our tidal model is quite sensitive to both these parameters. By assuming cyclostrophic balance we can relate latitudinal temperature gradients to vertical shear in the zonal wind (Schubert *et al.*, 1980). Above 70 km temperature measurements made by the OIR and the probes indicate that temperature increases poleward on constant pressure surfaces (Taylor *et al.*, 1980; Schofield and Taylor, 1983). According to cyclostrophic balance, this implies that the zonal wind will decrease with height. However, the vertical scale of the decrease and the extreme values reached are not well determined, because the mean zonal wind at 70 km is required as a boundary condition.

Above 60 km the model A profile is designed to provide a good fit to the OIR tidal data, and has zonal wind decreasing with height above 70 km. Below 60 km a vertically smoothed version of the day/night/sounder profile is used. The smoothing and increased shear in the lowest 10 km were necessary to avoid instabilities in the model.

Dissipation, in the form of Newtonian cooling and Rayleigh friction, was included in the model to absorb upward propagating waves. The physical basis for Newtonian cooling in the upper atmosphere is the damping of temperature perturbations by emission of infrared radiation to space. In general, the time required to damp a perturbation will decrease as the pressure decreases, as long as local thermodynamic equilibrium is maintained. A justification of the Newtonian cooling approximation for the cooling-to-space process is given by Pollack and Young (1975).

The results of several investigations into the infrared radiative cooling rates are presented in Fig. 5. In each of these investigations a detailed model of the radiative properties of the atmosphere was constructed and used to derive τ_N. In the model by Dickinson (1972), only cooling due to 15 μm bands of CO_2 was included; this model is most likely valid above the clouds, where the effects of water vapor and aerosols may be neglected. Pollack and Young (1975) included water vapor and aerosol effects, although both are somewhat uncertain. The profiles provided by Dr. Crisp (personal communication, 1981) are for a CO_2-only model and a CO_2-plus-cloud model. Our nominal profile for τ_R is also shown in Fig. 5. Since the profile of τ_R is not well constrained by models or observations, we have simply put $\tau_R \propto \sigma$. Below 90 km the solution is not sensitive to the value of τ_R, which is at least ten times greater than the value of τ_N at these altitudes.

The periodic forcing for the LPE model is derived from the daily variation in heating due to absorption of solar radiation. Most of the absorption takes place in the upper cloud region between 60 and 70 km. Data on this absorption were obtained by the *Pioneer Venus* Large Probe Solar Flux Radiometer (LSFR) (Tomasko *et al.*, 1980a). The LSFR measured the net flux in the spectral region 0.4 to 1.8 μm, from 65

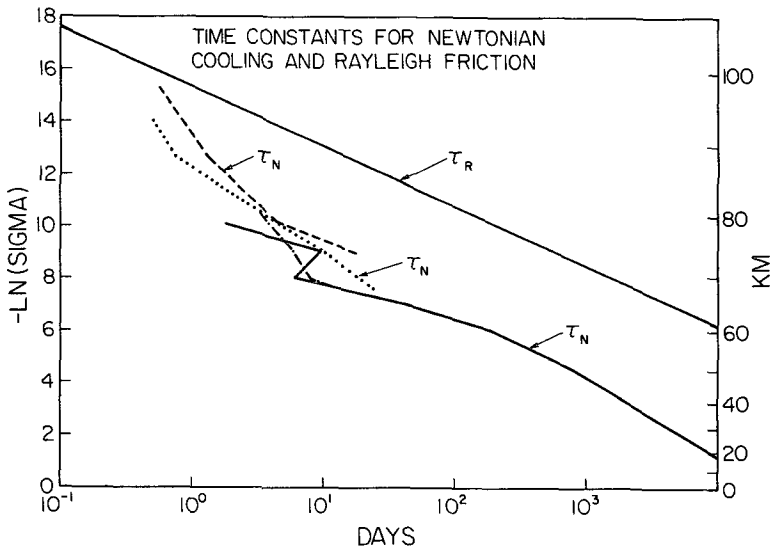

FIG. 5. The time constants of Newtonian cooling τ_N and Rayleigh friction τ_R. The profile of τ_N used in this study follows the solid curve of Pollack and Young (1975) up to 66 km altitude, then follows the dotted curve of D. Crisp (private communication, 1981) up to 80 km altitude and then follows the dashed curve of Dickinson (1972) up to 105 km where it intersects the τ_R curve. The dot-dash curve is Crisp's estimate of τ_N when the effects of cloud opacity are neglected.

km to the surface at a solar zenith angle of 65.7°. A model was constructed by Tomasko *et al.* (1980a) to estimate the globally averaged bolometric net flux from the data and to extrapolate the results to the top of the atmosphere. The heating rate at each level is proportional to the vertical derivative of the net flux. We assume that all the absorbed radiative energy goes directly into thermal energy.

Above the levels at which the LSFR operated, theoretical results predict large heating rates due to absorption of near infrared radiation by CO_2 (Dickinson, 1972). Since the heating rate peaks at 400 K d^{-1} at 120 km, this absorption provides a significant tidal forcing. Although the heating rates are large, the amount of energy absorbed is quite small, due to the low density at these altitudes.

In the LPE model the net bolometric solar flux F as a function of solar zenith angle θ_s and σ is given by

$$F(\sigma, \theta_s) = \begin{cases} \bar{F}(\sigma)A(n)\cos^n\theta_s, & \theta_s \leqslant \pi/2 \\ 0, & \theta_s \geqslant \pi/2, \end{cases}$$

where $\bar{F}(\sigma)$ is the globally averaged bolometric net flux and $A(n)$ is a normalization constant chosen so that the global average of F is $\bar{F}$. The vertical profile $\bar{F}(\sigma)$ is based on the LSFR data and on the work of Dickinson (1972).

At each level the heating rate is proportional to $d\bar{F}/d\sigma$, and can be resolved into a steady component and a variable component that has zero daily mean. We assume that the steady heating is balanced by a steady cooling due to infrared radiation and convection. Substituting $\cos\theta_s = \cos\lambda\cos\phi$ and determining the Fourier components of the ϕ dependence gives

$$\frac{\partial F(\sigma, \theta_s)}{\partial\sigma} = \frac{d\bar{F}(\sigma)}{d\sigma} A(n)\cos^n\lambda \sum_{m=0}^{\infty} B_m(n)e^{im\phi}.$$

The total tidal forcing is proportional to the above expression minus the $m = 0$ term. The $m = 1$ term gives the diurnal component of the forcing, the $m = 2$, the semidiurnal, etc.

An n of 1.6 gives the best fit to the values of the Tomasko *et al.* (1980a) model relation between the globally averaged flux and the flux at the sounder site from the ground up to 65 km. At the ground, where the net flux is approximately equal to the downward flux if the surface albedo is low, n may be estimated from the *Pioneer Venus* and *Venera* probe data, as is done by Tomasko *et al.* (1980b); this gives $n = 1.7$. In the LPE model we use $n = 1.6$ at all levels.

In the LPE model the global mean absorption of solar radiation $d\bar{F}/d\sigma$ is the sum of three terms. The first term is an analytic expression that fits the LSFR data in the vicinity of the clouds:

$$\frac{d\bar{F}_{\mathrm{LSFR}}}{d\sigma} = \frac{C_0}{(1 + \sigma/\sigma_0)^r}.$$

The corresponding heating rate is nearly constant high in the atmosphere, decreases rapidly below the clouds and is nearly zero in the lower atmosphere. The parameters C_0, σ_0 and r were determined by a nonlinear least-squares fit to the LSFR data for $\bar{F}$. For the best case $C_0 = -0.902145 \times 10^5$ W m^{-2}, $\sigma_0 = 0.122096 \times 10^{-2}$ and $r = 1.9$. With these values a total of 122 W m^{-2} is absorbed by the atmosphere in the vicinity of the clouds.

The second term represents the absorption of solar near-infrared radiation by CO_2 above the clouds. This term was modeled by an analytic expression

$$\frac{d\bar{F}_{\mathrm{IR}}}{d\sigma} = C_1 e^{-[|\eta-\eta_0|/d]^s},$$

where $\eta = -\ln\sigma$ and η_0 is $-\ln\sigma$ at 120 km. If $C_1 = -3.54 \times 10^6$ W m^{-2}, the heating rate is 400 K d^{-1} at 120 km. Values of 3.1 for d and 1.5 for s were chosen for the LPE model to give a good fit to the theoretical curve of Dickinson (1972). These values give a total absorption of about 5 W m^{-2}.

Finally, a net flux of $\bar{F}_{\mathrm{BL}} = 17$ W m^{-2} at $z = 0$ is absorbed by the ground (Tomasko *et al.*, 1980a). This absorption will heat the surface which will, in turn, heat the atmospheric boundary layer. The heat will be distributed over the lower atmosphere by convection, radiation and/or conduction. This heat will also contribute to the tidal forcing. Unfortunately, not enough is known about the state of the lower atmosphere to constrain its distribution very well. We have studied the effects of this heating in various cases. If the stability near the ground is low, as in our nominal basic state, there is only weak propagation of this wave energy into the upper atmosphere. Also, if the heating is confined to the lowest level in the model, the tidal response to this heating falls off rapidly with height, independent of the stability. Heating at the ground is not included in our nominal model. However, this heating is important locally, so our nominal solution is incomplete in the lowest layers.

4. Results

In this section the *Pioneer Venus* OIR data are compared to the LPE model results for the nominal basic state described in the previous section. To do this we must first model the range of altitude sampled by each OIR channel.

The weighting functions of the OIR channels, which represent the altitude distribution of radiation reaching the detectors are shown in Fig. 6. These curves were supplied by Elson (personal communication, 1982) and were calculated from theoretical models of infrared opacity in the Venus atmosphere. Channel 5 is located in a spectral window of low CO_2 absorption at 11.5 μm and is sensitive to temperatures near the cloud tops. The channel 5 weighting function

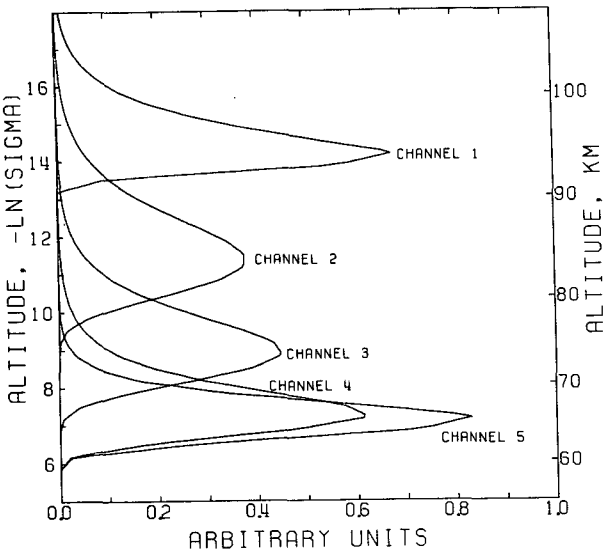

FIG. 6. Weighting functions used to obtain model brightness temperatures for comparison with those measured in the OIR channels. A table of weighting function values computed from an opacity model was provided by L. Elson (private communication, 1982). Similar weighting function values were used by Schofield and Taylor (1983).

depends on the height of unit optical depth of the cloud particles and on their scale height. The weighting function for channel 4 is also somewhat affected by cloud opacity.

Taylor *et al.* (1980) and Elson (1983) Fourier analyzed the OIR brightness temperatures with respect to solar-fixed longitude to determine the OIR tidal signals. Elson (1983) analyzed the brightness temperatures in channels 2–5. These recent results are more reliable than those in Taylor *et al.* (1980) because the final data set included more observations and had improved geometry. The results for channel 1 from Taylor *et al.* (1980) must be considered more uncertain.

The OIR tidal results for channels 2–5 (Elson, 1983) are shown in Figs. 7–14. These figures contain plots of observed brightness temperature amplitude and phase versus latitude for both the diurnal and semidiurnal tide. Although it is difficult to determine error bars, near the equator the amplitudes are probably accurate to within one or two degrees, and the phase is good to an hour or two (Elson, personal communication, 1982). The accuracy is better in the polar regions because of better OIR coverage. Curves from the nominal model of this paper are also shown in Figs. 7–14. The model brightness temperatures were obtained by converting the model temperatures to radiances and then convolving with the weighting functions to obtain the brightness temperature. Due primarily to lack of structure in the model basic state in the polar regions and also to lack of resolution in the three-term spherical harmonic expansion of the model tidal fields, the disagreement between the model and the data is most serious poleward of 50°.

In Tables 1–4 the observed and model values for amplitude and phase of the brightness temperature variations are compared quantitatively at two latitudes. Phase is given in terms of local solar time by specifying the hour of maximum temperature. Semidiurnal and diurnal phases are given in terms of 12 hour and 24 hour clocks, respectively.

The model tidal temperature perturbations used to calculate the model brightness temperature amplitudes and phases are shown at two latitudes in Figs. 15–18. The points on the figures give the values at each level of the vertical grid, thus giving a rough idea of the adequacy of the vertical resolution. The grid points are equally spaced in $-\ln\sigma$. Doubling the vertical resolution (reducing the vertical step size) in the semidiurnal case had very little effect on the solution. This test was not done for the diurnal case, but errors are expected to be low (Pechmann, 1983). Similarly, increasing the horizontal resolution by increasing the number of terms in the Legendre

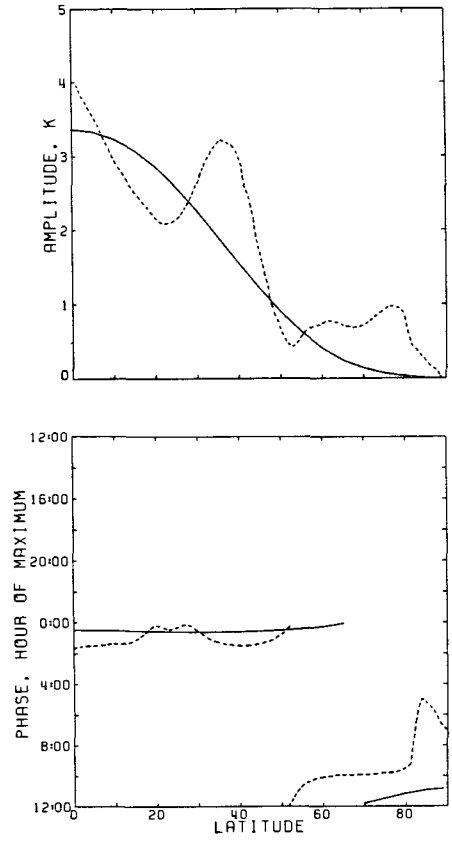

FIG. 7. Semidiurnal amplitude and phase in OIR channel 2 from the LPE model A (solid curve) and from the measured OIR brightness temperatures (dashed curve). Fourier analysis of the OIR data (Figs. 7–14) was done by Elson (1983).

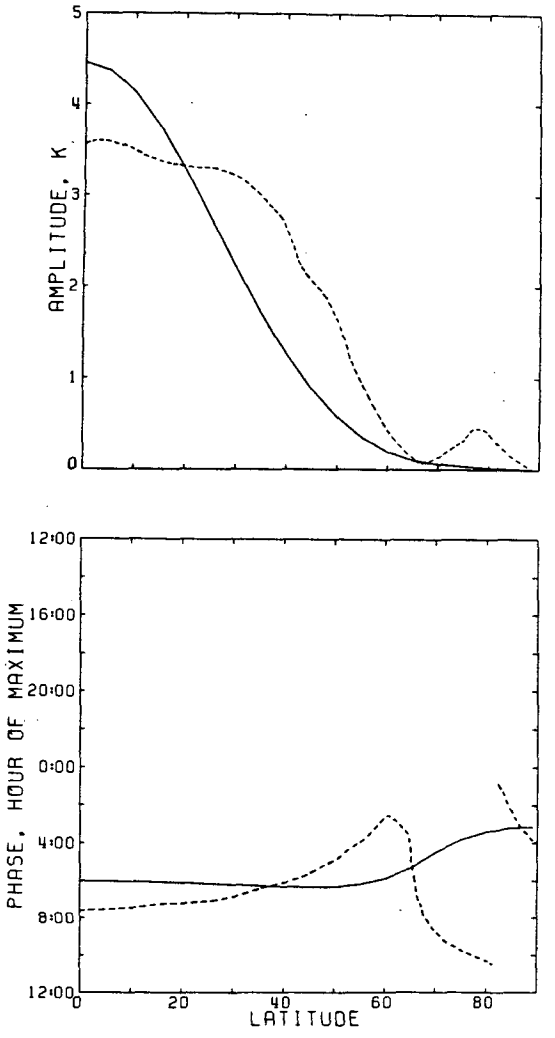

FIG. 8. As in Fig. 7 but for OIR channel 3.

expansion from 3 to 5 (and the number of Gaussian grid points from 7 to 12) had little effect except for the diurnal tide at high latitudes, although the solutions were not run for as many time steps at the higher resolutions. The diurnal tide is trapped at high latitudes in the high resolution case. The adequacy of the convergence is illustrated by giving the solution at the final time step and at half the total number of time steps. A summary of the numerical parameters in the nominal model is given in Table 5.

As shown in Tables 1 and 2, the phase of the semidiurnal tide does not change much with height in the three lowest altitude channels, suggesting either that the wavelength is extremely long or that the wave is damped or trapped. In the latter case there are three possibilities: 1) trapping due to a frequency less than twice the vertical component of the rotation vector, 2) trapping due to low static stability, or 3) suppression of propagation by damping. None of these situations is likely to prevail in the altitude range 60–80 km on Venus (Pechmann, 1983). Moreover, if the wave were damped or trapped the hour of maximum temperature should lag the hour of maximum solar heating according to classical tidal theory, yet a phase lead (i.e., a decrease in the hour of maximum temperature) is observed (Taylor *et al.*, 1980; Schofield and Taylor, 1983).

The complete explanation can be seen in Figs. 15 and 16. Wave trapping occurs only in the altitude ranges 50–55 km and above 90 km. At 50–55 km the semidiurnal maxima of temperature at 0300 and 1500 lag the semidiurnal maxima of solar heating at noon and midnight, as expected for a trapped wave. Above 55 km wave energy propagates upward and wave phase propagates downward. This causes the hour of maximum temperature to decrease with

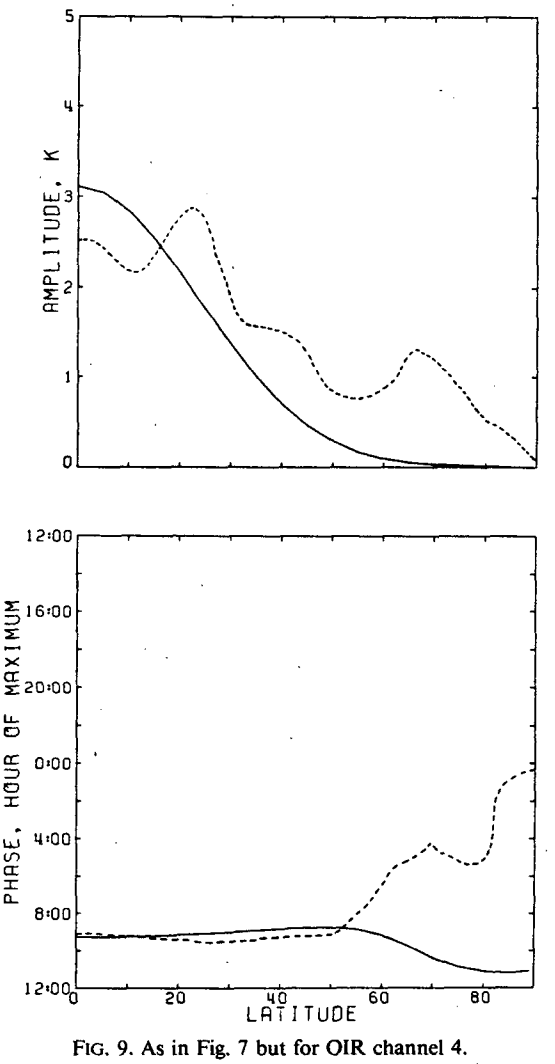

FIG. 9. As in Fig. 7 but for OIR channel 4.

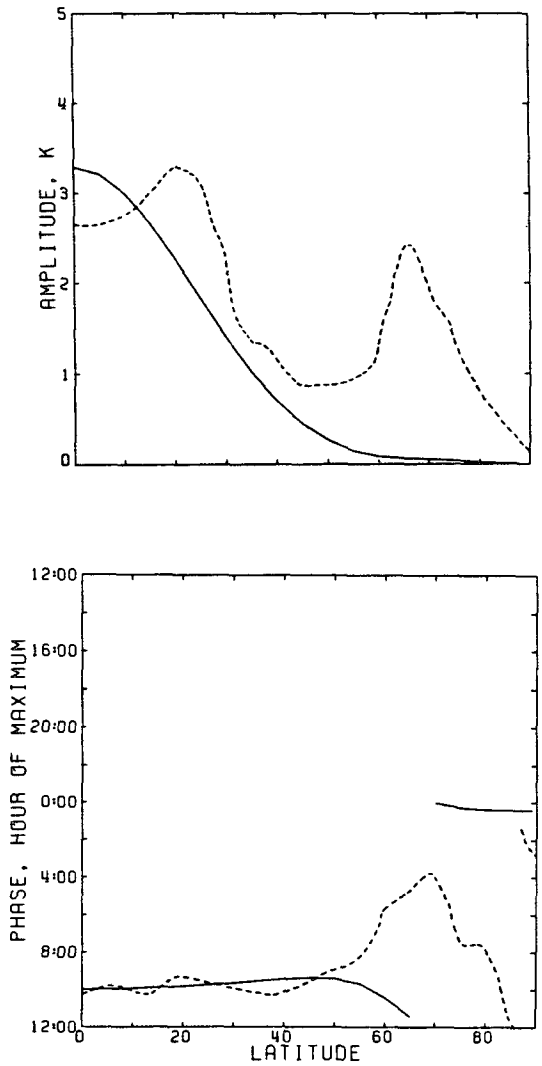

FIG. 10. As in Fig. 7 but for OIR channel 5.

altitude, such that lines of constant phase slope upward to the right. This phase decrease with height for an upward propagating wave is one of the peculiarities of gravity waves; a nondispersive wave in an isotropic medium would give a phase increase with height. By the time the wave reaches the levels sampled by channels 3–5 at 65–75 km, it leads the sun by 3 hours with maxima around 2100 and 0900. Since the wavelength is long at these altitudes, the phase does not change much from one channel to the next. Between 80 and 90 km the wavelength decreases due to increasing stability and decreasing zonal wind, causing a large phase decrease from channel 3 to channel 2.

The wave does not propagate near 50–55 km because the static stability is low. In this layer the terms involving γ^* in the thermodynamic equation are negligible, so the zonal advection and the forcing nearly balance:

$$im\Omega T' \approx Q'.$$

Here the phase of T' lags the phase of Q' by $\pi/2$ so the semidiurnal maxima of temperature are at 0300 and 1500.

Above 90 km the model response is damped by Newtonian cooling and Rayleigh friction which cause the maxima to be near 1200, in phase with the forcing. Other models in which the wave continues to propagate above 90 km might, by coincidence, give a channel 1 phase near 1200. The damped model is preferred however, because the amplitude is close

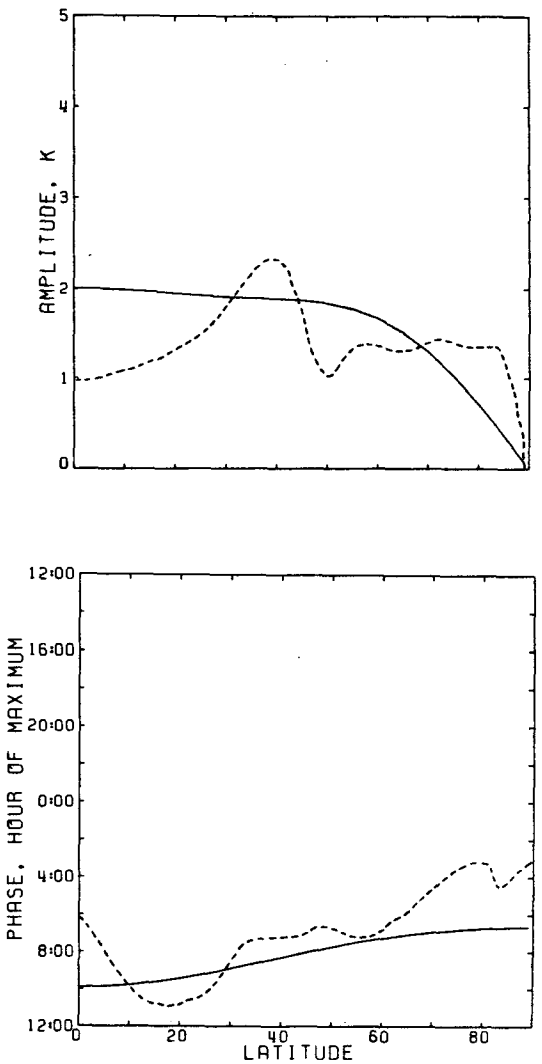

FIG. 11. As in Fig. 7 but for the diurnal tide. The amplitude and phase are shown here for OIR channel 2. The solid curve is from the model, and the dashed curve is from the measurements.

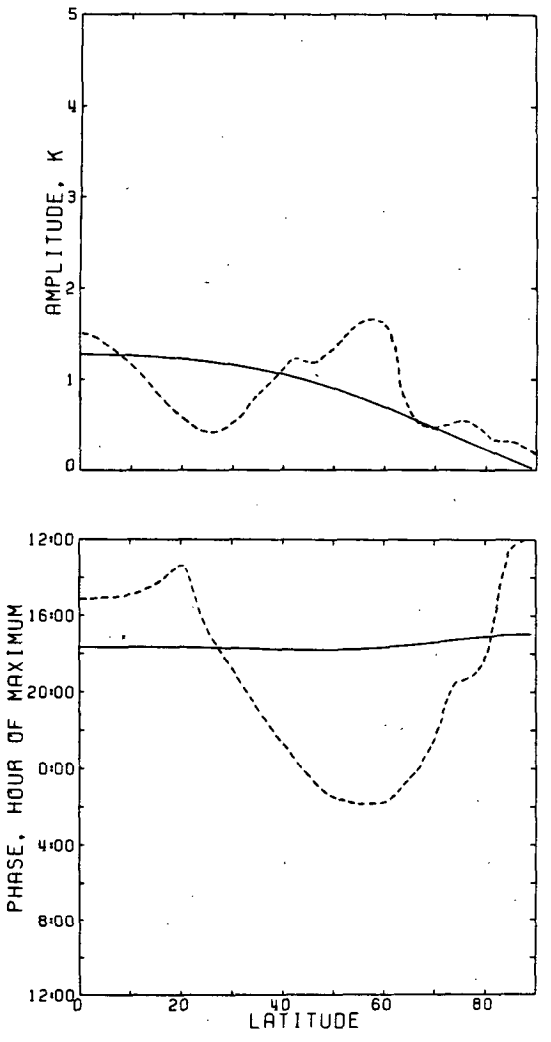

FIG. 12. As in Fig. 11 but for OIR channel 3.

to the OIR amplitude, and the values assumed for the radiative damping (Fig. 5) are realistic.

The other question about the OIR tidal data concerns the relative amplitude of the diurnal and semidiurnal brightness temperature perturbations—the observed diurnal amplitude is smaller than the semidiurnal amplitude in channels 2–5 from the equator to 50°. The relatively low diurnal amplitude occurs even though the diurnal forcing is about twice as great as the semidiurnal. Also, for thermally forced gravity-type waves, the amplitude of the temperature perturbation is inversely proportional to the frequency. Thus, the diurnal amplitude would exceed the semidiurnal amplitude by about a factor of 4 if the frequency and the forcing were the only contributing factors.

There are two parts to the explanation of the relatively low diurnal amplitude. First, the diurnal amplitude of the brightness temperature perturbation is less than the amplitude of the actual temperature perturbation from which it is calculated. This reduction occurs because the diurnal tide at 60 to 90 km is characterized by an upward propagating wave with a vertical wavelength of about 7 km, as shown in Figs. 17 and 18. Since the width of the OIR weighting functions is between 5 and 10 km, the convolution of the model temperatures and the weighting functions results in a significant amount of cancellation. The semidiurnal tide also propagates in this region, but with a much longer vertical wavelength. Second, the model diurnal temperature amplitude is not four times the semidiurnal over most of the altitude range covered by the OIR. In fact, at the equator the two are nearly equal from 60 to 80 km. It seems likely that the diurnal response is somewhat suppressed for the same reason the terrestrial diurnal tide is weak

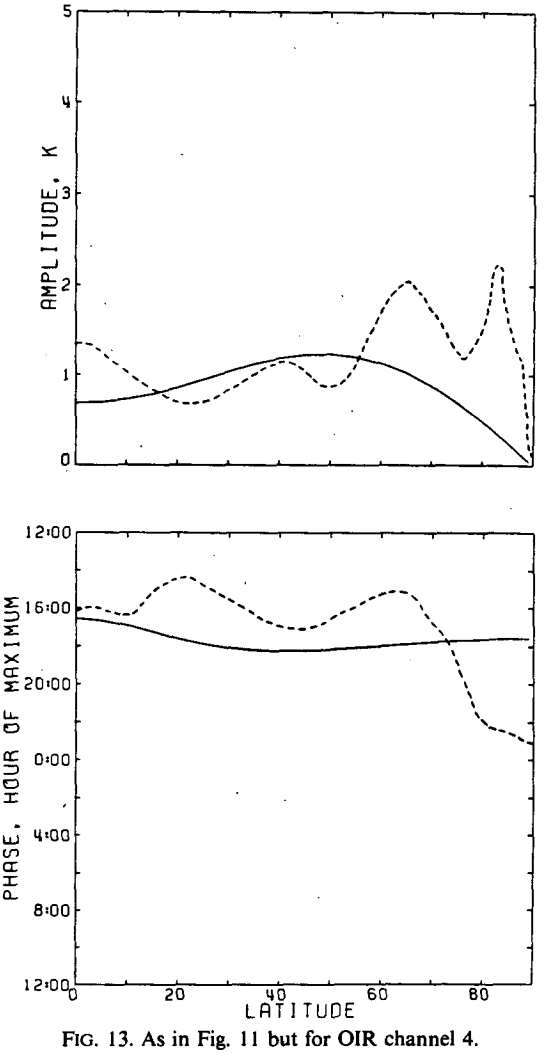

FIG. 13. As in Fig. 11 but for OIR channel 4.

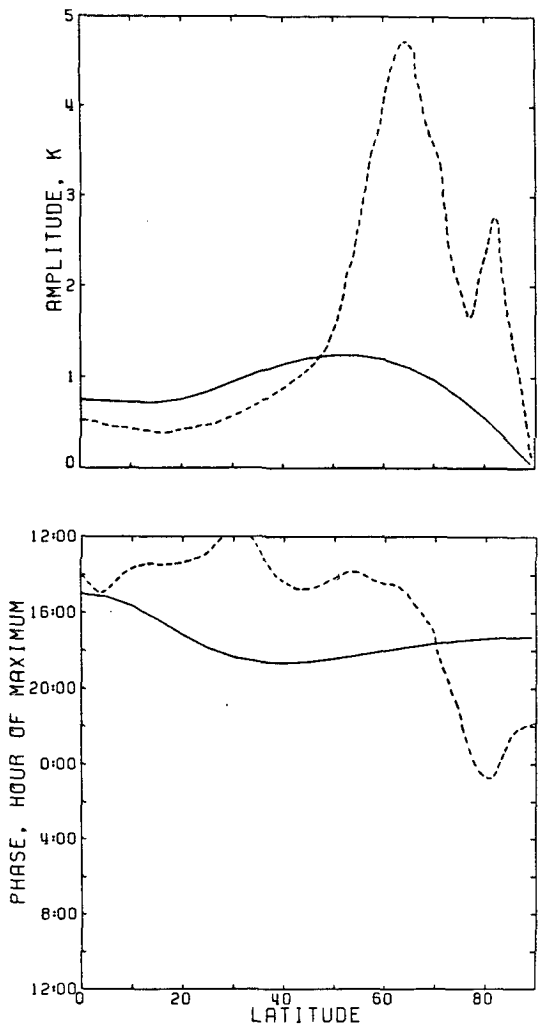

FIG. 14. As in Fig. 11 but for OIR channel 5.

(Chapman and Lindzen, 1970). Since the forcing is spread out over more than a diurnal wavelength, destructive interference takes place between waves excited at different levels. The semidiurnal wavelength is longer, so the atmosphere responds more coherently at this frequency. The semidiurnal wavelength in the region of the forcing is about 30 km, four times the diurnal wavelength, which might be enough to equalize the response at the two frequencies.

Why is the wavelength of the diurnal tide smaller than that of the semidiurnal tide? The dispersion relation for two-dimensional gravity waves predicts that the vertical wavelength for the diurnal and semidiurnal tides should be the same. For such a gravity wave the vertical wavelength depends on static stability and phase speed but not on frequency (Holton, 1979). Since the two-dimensional gravity wave theory is inadequate, the difference must come about because of the meridional structure of the tides. A simple argument will illustrate this dependence.

The dispersion equation for long gravity waves in a fluid with constant Brunt–Vaisala frequency N^2 is

$$m^2 = N^2(k^2 + l^2)/\omega^2$$

(e.g., Holton, 1979), where ω is the frequency, k and l are the horizontal wavenumbers and m is the vertical wavenumber. For a wave propagating at velocity $\bar{u}$ in the direction of the k wavenumber, we have $\omega^2 = \bar{u}^2k^2 \approx \bar{u}^2n^2/r^2$. Here we let $n = 1$ or 2 for diurnal and semidiurnal tides, respectively, and we let k be of order n/r, where r is the planetary radius. The north–south wavenumber l is of order $1/r$ for both the diurnal and the semidiurnal tides. Thus, l^2 is relatively more important in the dispersion equation for the diurnal tide, and less important for the semidiurnal tide, since ω^2 and k^2 both contain a factor of n^2. The effect of l^2 is therefore to raise the value of m^2 for the diurnal tide. Increasing the horizontal resolution in the LPE model did not

TABLE 1. Semidiurnal tide at the equator.

Channel	Height (km)	Amplitude (deg) OIR	Amplitude (deg) Model	Phase (h_{max}) OIR	Phase (h_{max}) Model
1	100	6.0	4.9	1200	1158
2	90	4.0	3.5	0140	1227
3	80	3.7	4.4	0740	0554
4	70	2.5	3.1	0900	0916
5	cloud tops	2.6	3.3	1000	1000

TABLE 2. Semidiurnal tide at 40°.

Channel	Height (km)	Amplitude (deg) OIR	Amplitude (deg) Model	Phase (h_{max}) OIR	Phase (h_{max}) Model
1	100	3.7	3.0	0100	1157
2	90	2.9	1.5	0140	1229
3	80	2.6	1.2	0615	0611
4	70	1.5	0.7	0915	0849
5	cloud tops	1.2	0.7	1000	0926

TABLE 3. Diurnal tide at the equator.

Channel	Height (km)	Amplitude (deg) OIR	Amplitude (deg) Model	Phase (h_{max}) OIR	Phase (h_{max}) Model
1	100	10.0	17.4	1000	1159
2	90	1.0	2.0	0600	0948
3	80	1.5	1.3	1500	1736
4	70	1.3	0.7	1600	1634
5	cloud tops	0.5	0.7	1400	1500

TABLE 4. Diurnal tide at 40°.

Channel	Height (km)	Amplitude (deg) OIR	Amplitude (deg) Model	Phase (h_{max}) OIR	Phase (h_{max}) Model
1	100	8.0	12.8	1000	1159
2	90	2.3	1.9	0715	0816
3	80	1.1	1.0	2245	1744
4	70	1.2	1.2	1700	1814
5	cloud tops	0.9	1.1	1415	1839

change this difference between the diurnal and semidiurnal wavelengths.

Overall, the agreement between the LPE model and the OIR data is quite good for the diurnal amplitudes and phases (see Tables 3 and 4). This agreement is remarkable because all the fine adjustments of the basic state were made to optimize the fit to the semidiurnal amplitudes and phases. The good agreement between the model and the OIR for the diurnal amplitudes and phases may be considered an independent check of the validity of the model. The agreement in the diurnal phase is especially significant because the diurnal wavelength is so short. Small changes in the basic state could cause a significant change in the phase of the brightness temperature perturbation. The phase in channels 4 and 5 would also be sensitive to variation in the cloud properties which would alter the weighting functions.

Evidence that the diurnal phase is difficult to determine from observations is given by Diner *et al.* (1982). They review the ground-based observations of solar-locked components in the infrared emission and compare them to the OIR results. The ground-based observations are in the 11 μm region, so they are compared to the OIR's channel 5. The semidiurnal amplitude and phase and the diurnal amplitude determined from the entire data set agree well with those based on the OIR channel 5 data alone. However, the diurnal maximum determined from the entire data set is at about 0400, whereas the OIR diurnal maximum in channel 5 is at 1400. Diner *et al.* (1982) interpret this discrepancy as being due to inadequate longitudinal coverage by the OIR. It is also possible that the discrepancy is caused by the different spectral passbands of the ground-based and spacecraft observations. Because of the short diurnal wavelength, caution should be exercised in comparing results from instruments with different weighting functions.

Caution is also required in interpreting retrieved temperature profiles, again because of the short diurnal wavelength. Figure 10 of Schofield and Taylor (1983), which is reproduced as Fig. 4 of Taylor *et al.* (1983), is a good example. These authors inverted the convolution of weighting functions and radiance profiles to solve for the latter, and, hence, inferred a temperature profile. Since the weighting functions are broad (e.g., Fig. 6), the retrieved temperature profile is a smoothed version of the true profile. Viewed in this way, there is no inconsistency between Fig. 10 of Schofield and Taylor, which shows the retrieved temperature field versus altitude and solar longitude, and our tidal theory. Lindzen and Teitelbaum (1984), however, did not consider this smoothing in their analysis of Schofield and Taylor's retrieved profiles.

Of the instruments on *Pioneer Venus,* only the OIR obtained a data set of sufficient spatial and temporal extent to detect tidal oscillations in the Venus stratosphere. In general, our tidal results should be consistent with other more limited data sets, although there are a few exceptions. For example, Fig. 19 shows the model temperature profile, including the diurnal and semidiurnal components, at the sounder site. The oscillations between 65 and 90 km are caused by the solar tide. This profile may be compared to that obtained by Seiff *et al.* (1980) from the probe accelerometer data. The observed sounder profile does not show the predicted oscillations. The tidal signal may have been lost due to the low vertical resolution of the measurements, about 3 km. Thus, most of the amplitude of the diurnal tide may have been smoothed out. The predicted tidal oscillations at the other probe sites are too small to have been observed above the noise level of the data.

The temperature profiles of the Venus stratosphere obtained by radio occultations have a vertical resolution of about 1 km (Woo *et al.,* 1980). Kliore and Patel (1980) have published numerous profiles ranging from equatorial to polar latitudes. The altitude range covered by these profiles is 50–80 km. Most of the profiles show wavelike structure between 60 and 80 km. The most prominent wavelength is approximately 5 km, somewhat shorter than the 7 km predicted for the diurnal tide. The observed amplitude is com-

TABLE 5. Numerical parameters.

	LPE diurnal	LPE semi-diurnal	Gravity wave semi-diurnal
Number of vertical points	218	110	110
Top of resolved region ($-\ln\sigma$)	18	18	18
Number of terms in Legendre expansion	3	3	—
Number of points in Gaussian latitude grid	7	7	—
Time step (s)	14 400	7200	14 400
Number of time steps	1200	1600	800

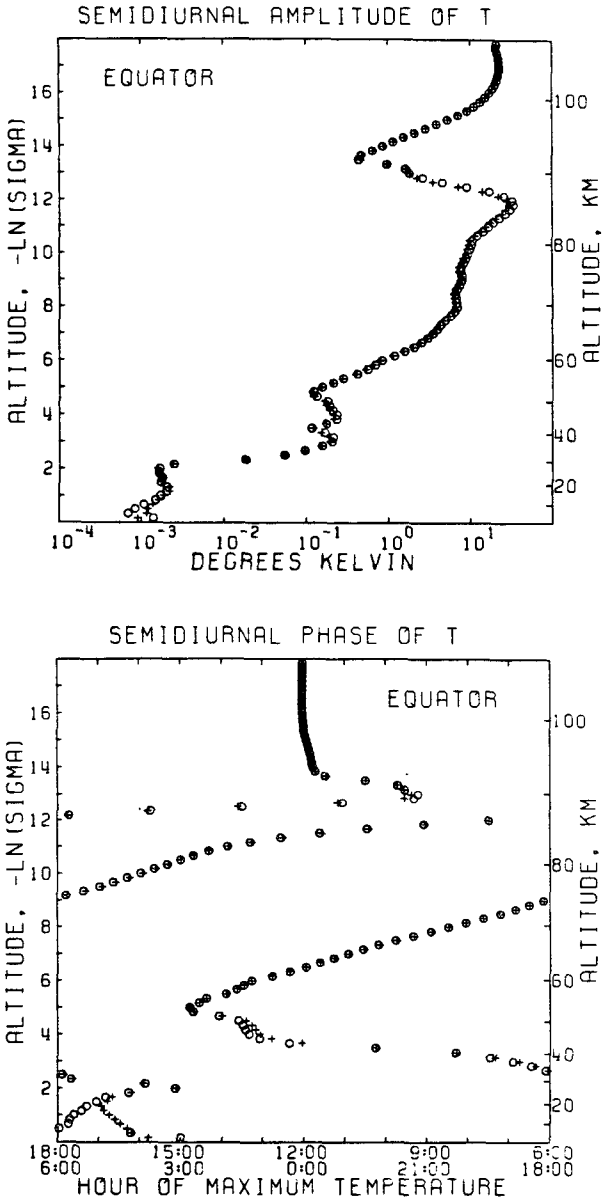

FIG. 15. Semidiurnal tide at the equator for the nominal LPE model. The upper part shows the amplitude of the temperature oscillation as a function of height; the lower part shows the phase of the oscillation. The pluses show the solution after 800 time steps; the circles show the solution after 1600 time steps. For other parameters of the nominal model, see Table 5.

parable to the model amplitude at mid to high latitudes, but is smaller at low latitudes.

Finally, we compare our tidal meridional velocities (Fig. 20) to those measured by the *Pioneer Venus* DLBI experiment (Counselman *et al.*, 1980). The amplitude of vertical variations in the model tidal velocities is consistent with those in the measured profiles. In fact, the tides may be responsible for some of the structure seen in the data above 40 km. The wavelengths are nearly the same, but the phase does not agree very well. Other components of the circulation, such as synoptic eddies and mean meridional flows, may also be contributing to the observed velocities.

5. Sensitivity studies

The model brightness temperatures are sensitive to changes in the basic state and forcing. Examples of this sensitivity are shown in Fig. 21 and Table 6, at 800 time steps. In Fig. 21 we show the results of running the LPE model with the profile of Γ^* labeled model B in Fig. 3. The solutions for model A (solid line) and B (dotted line) are very similar; the major

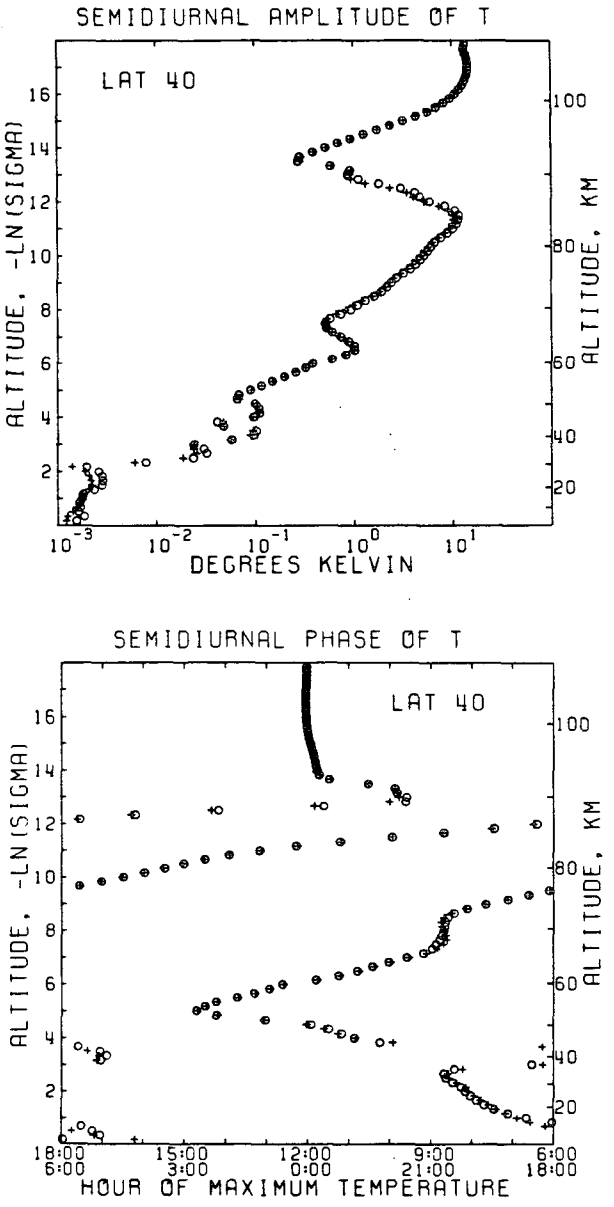

FIG. 16. As in Fig. 15 but for latitude = 40°.

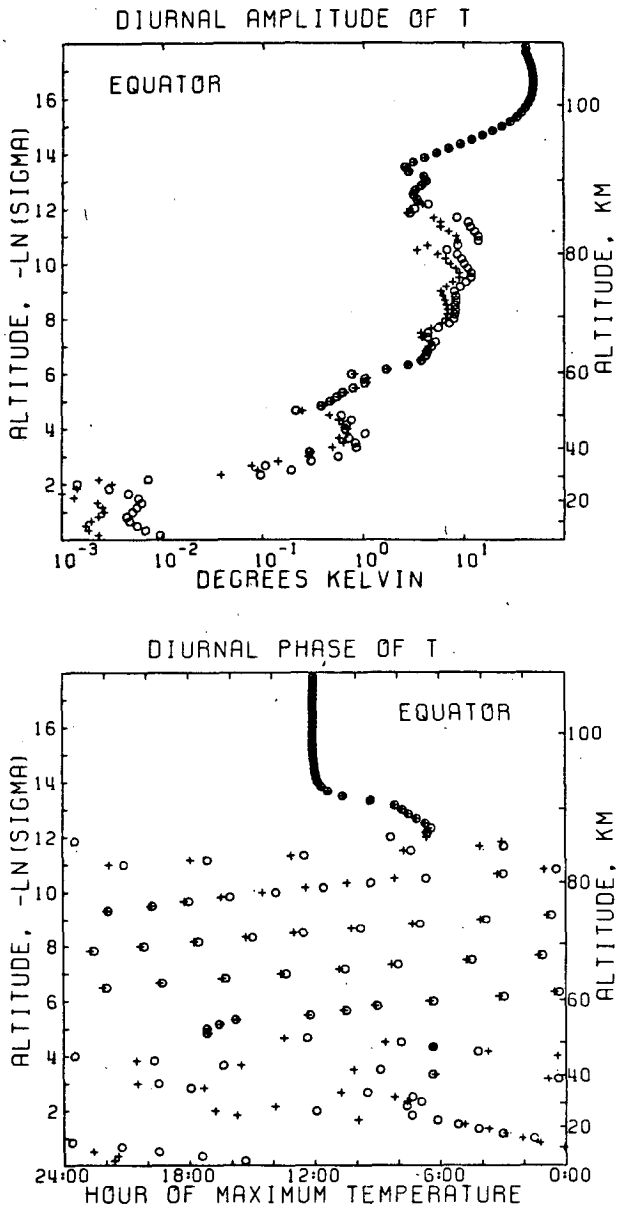

FIG. 17. As in Fig. 15 but for the diurnal tide. Here the pluses show the solution after 600 time steps, and the circles show the solution after 1200 time steps.

change is in the phase below 70 km. The semidiurnal brightness temperature amplitudes and phases at the equator in the OIR channels for model B are given in Table 6. The modification of Γ^* in model B does not result in large changes from model A. The same is not true when the maximum equatorial wind is reduced to 98 m s^{-1} from 122 m s^{-1}. This profile of the mean zonal wind is labeled model C in Fig. 4; the corresponding solution to the LPE model is shown as a dashed line in Fig. 21. The general vertical structure is unchanged, but the amplitudes and phases in the OIR channels, given in Table 6, are significantly different from model A and tend to agree less well with the OIR data. The values are affected because the vertical wavelength from 65 to 90 km is shorter than in model A. Because of the averaging effect of the weighting functions, the shorter wavelength causes the amplitudes in the OIR channels to decrease. Also, the phase as a function of height is affected by the change in wavelength. It may be possible to get as good agreement with the OIR data by varying u^* and Γ^* together. However, Γ^* may not be changed arbitrarily since the temperature profile must be realistic.

Additional sensitivity studies have been done using the gravity wave model described in Section 2. The

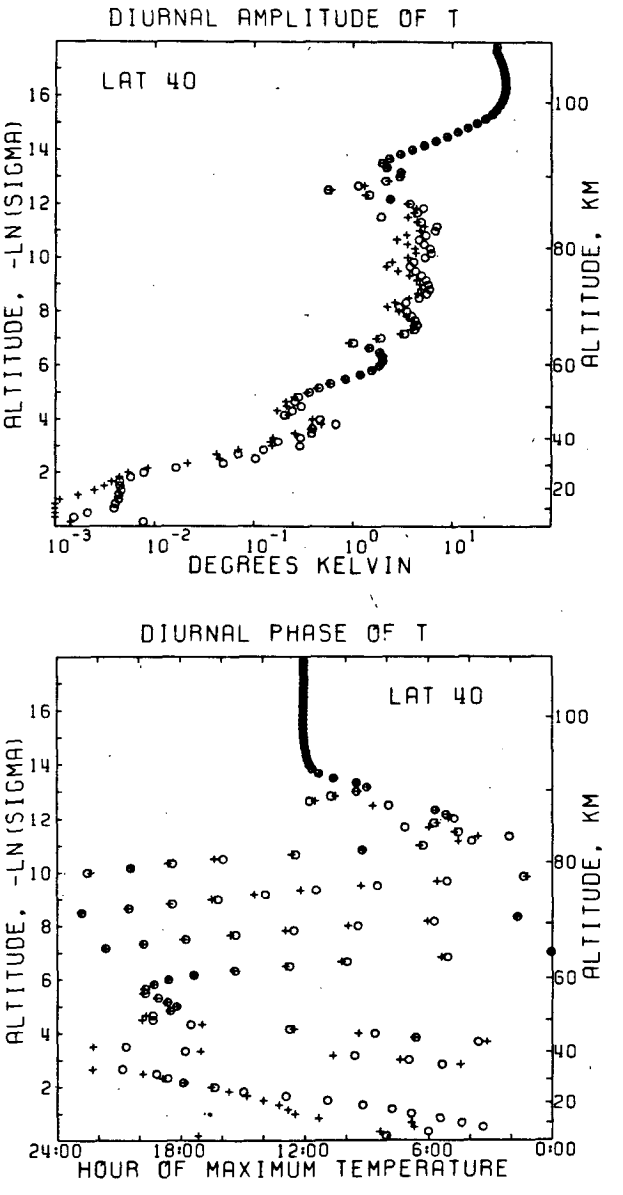

FIG. 18. As in Fig. 17 but for latitude = 40°.

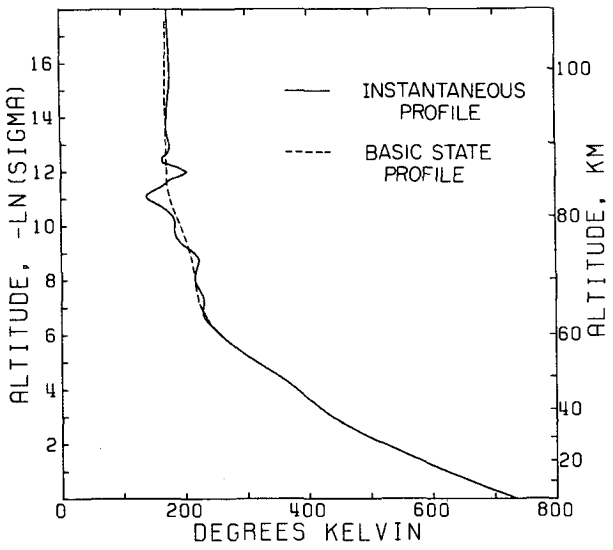

FIG. 19. Temperature profile at the *Pioneer Venus* sounder probe site computed from the LPE model. The instantaneous diurnal and semidiurnal tidal fields have been added to the basic state temperature profile (dashed curve) to produce the solid curve.

numerical parameters for this model are given in Table 5. In Fig. 21 we compare the gravity wave solution for the semidiurnal tide (dot-dashed line) to that of the LPE model at the equator for model A, the nominal basic state and forcing. The amplitudes and phases from the two models are in good qualitative agreement. Similar agreement between the models is obtained for models B and C (Pechmann, 1983). Thus, the gravity wave model shows the same degree of sensitivity as the LPE model to changes in the input parameters. The gravity wave model does not give as good an approximation for the diurnal tide so results for just the semidiurnal tide will be presented. The greater amplitude of the diurnal tide at higher latitudes (Figs. 7–14) makes the separability approximation of the gravity wave model less valid.

In Fig. 22 we explore the sensitivity of the solution to changes in the basic state using the gravity wave model. We compare the nominal case (solid line) to a case (dotted line) that has constant shear with respect to $\ln\sigma$ below 70 km (model D in Fig. 4). This change has very little effect on the solution except on the phase below 30 km. The solution is less sensitive to the details of the u^* profile below 70 km than to the value of the peak zonal wind. The dashed curve is for a case in which the zonal wind is constant at 125 m s^{-1} above 75 km (model E in Fig. 4). The wavelength above 75 km is increased, which would significantly affect the amplitude and phase of the brightness temperature in OIR channels 1–3. The solution is not completely damped at high altitudes because the sponge layer is less effective when τ is a larger fraction of the local diurnal period. However, it may be possible, by adjusting the damping and the static stability, to reach agreement with the OIR data for a basic state with some degree of super-rotation above 90 km.

Just before the *Pioneer Venus* probes failed, they observed increasing static stability as they descended (Seiff *et al.*, 1980). The dot-dashed curve (model F)

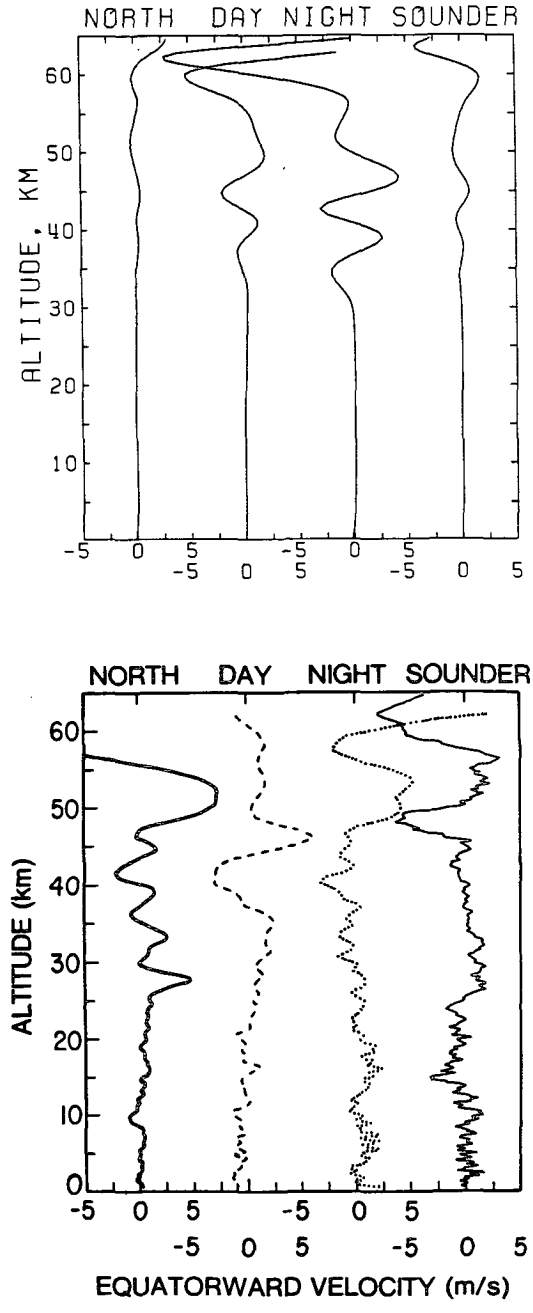

FIG. 20. Meridional wind at each of the *Pioneer Venus* probe sites computed from the LPE model (top) and observed by the DLBI experiment (Counselman *et al.*, 1980) (bottom). The instantaneous tidal fields were used to produce the computed curves.

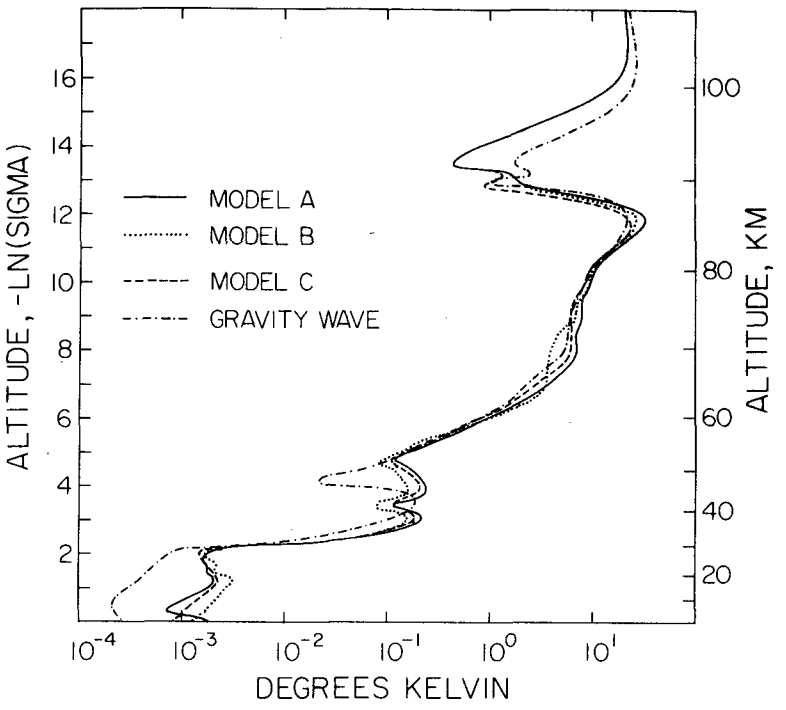

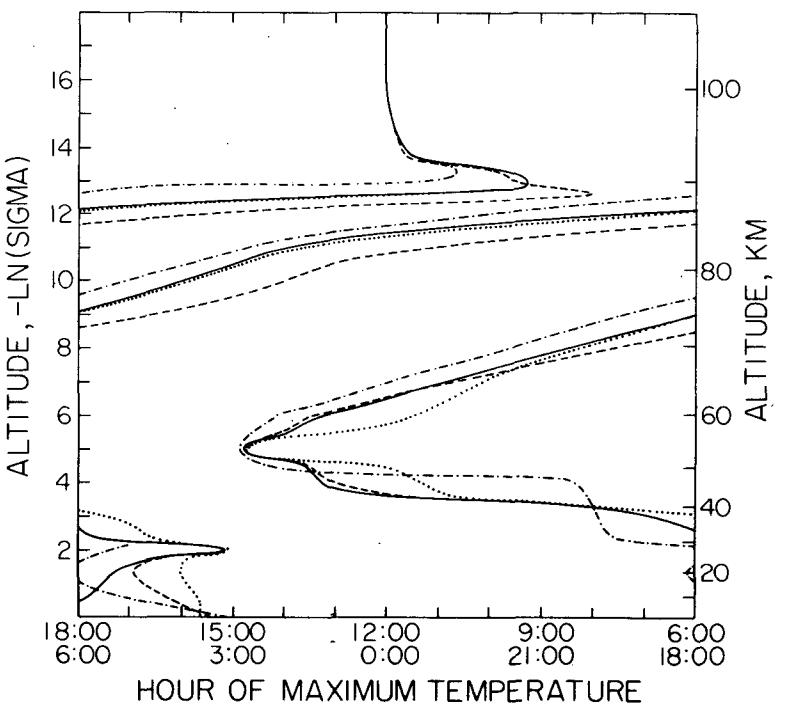

FIG. 21. Semidiurnal temperature oscillation at the equator for different input parameters. The solid curve is for the nominal model A described in Figs. 3–5 and Tables 1–5; and was computed using the LPE model. The dotted curve is for the alternate model B whose static stability profile is shown in Fig. 3, and was also computed using the LPE model. Except for the profiles of Γ^*, T^* and C_p^*, the two models have the same input parameters. The dashed curve used the zonal velocity profile C of Fig. 4, and was also computed using the LPE model; otherwise, its input parameters are the same as model A's. The dot-dash curve was computed using the gravity wave model with the input parameters of model A. When the nominal model curve overlies one of the other curves in Figs. 21–23, only the nominal curve is shown.

TABLE 6. Sensitivity of LPE model to basic state parameters for semidiurnal tide at the equator.

	Channel	Amplitude (deg)	Phase (h_{max})
OIR	1	6.0	1200
	2	4.0	0140
	3	3.7	0740
	4	2.5	0900
	5	2.6	1000
Nominal basic state (model A)	1	4.8	1158
	2	3.5	1229
	3	3.8	0553
	4	2.7	0913
	5	2.9	0956
Modified Γ^* profile (model B)	1	4.9	1158
	2	3.0	1216
	3	3.6	0524
	4	2.7	0908
	5	3.1	0941
Maximum u^* = 100 m s^{-1} (model C)	1	4.9	1158
	2	1.7	1036
	3	2.9	0424
	4	2.2	0835
	5	2.4	0926

in Fig. 22 shows the effects of higher stability near the ground, such that $\Gamma^* = 0.5$ K km^{-1} below 30 km (Fig. 3). Model F was run for 1600 time steps because the higher stability slows down the convergence. Below 30 km the amplitude is greatly increased, and the phase is seriously affected. Thus, the tidal perturbations near the ground cannot be determined accurately until the static stability there is known. Fortunately, the solution above 30 km is not sensitive to this change in Γ^*.

We have used the time constant for Rayleigh friction τ_R to model small-scale momentum dissipation, but its value was chosen somewhat arbitrarily. If the damping by Rayleigh friction is negligible, the solution below about 90 km is unaffected as shown in Fig. 23 (dotted curve). Thus, the sponge layer seems to work with Newtonian cooling alone. However, to match the amplitude and phase in channels 1 and 2, some amount of Rayleigh friction is needed.

The forcing in the nominal case smoothly approaches zero in the lower atmosphere. Figure 23 (dashed curve) shows a step function distribution of the heating. The heating rate is constant above $-\ln\sigma = 7$ and zero below that level. In this case, a standing wave is set up below the step. The lower amplitude in the sponge layer in the case of the step function is due to the constant heating rate. In the standard case, the heating rate increases with height because of the near-IR absorption.

In Fig. 23 (dot-dashed curve) we show the results when the 17 W m^{-2} of heating near the ground is included as a δ-function in the lowest model level. This solution agrees well with the nominal case above 20 km. Near the ground the amplitude and phase cannot be determined accurately, not only because of the uncertainty in Γ^* discussed above, but also because of the unknown vertical distribution of the heating.

Dobrovolskis and Ingersoll (1980) used a gravity wave model similar to ours to calculate Venus thermal tides. The results were used to estimate the torque that the sun exerts on the atmosphere due to the tidal redistribution of mass. This torque may be transmitted to the solid planet by friction and may play an important role in maintaining the planet's rotation. The torque is proportional to $\mathrm{Im}(p_s')_2$, the imaginary part of the semidiurnal surface pressure oscillation. Table 7 gives $\mathrm{Im}(p_s')_2$ calculated from the gravity wave model for various heating distributions. The result for the δ-function are consistent with DI if our result is scaled by their values of heating, surface temperature and specific heat. However, our model shows greater sensitivity to changes in the distribution, i.e., when the heating near the ground is spread out in height in the diffusion model, the analytic form of which is given by DI. In the case given in Table 7, the thermal skin depth equals the atmospheric scale height. In their model the difference in $\mathrm{Im}(p_s')_2$ between the δ-function model and the diffusion model is about a factor of 2, while in our model it is a factor of 5. The discrepancy is probably due to differences in the basic state. Near the ground DI's atmosphere is adiabatic, while ours has a small positive static stability. We also have more shear in the zonal wind near the ground. Nevertheless, in agreement with DI, we find that the torque generated by heating in the clouds is negligible compared to that generated by heating near the ground, as is shown in the final two entries in Table 7.

The model brightness temperatures are also sensitive to changes in the cloud parameters which determine the shape of the weighting functions in channels 4 and 5. These weighting functions were computed by Elson (personal communication, 1982). Cloud structure can be characterized by H_c, the ratio of the cloud particle scale height to the gas scale height, and by p_c, the pressure at which optical depth unity is reached; p_c could lie between 50 and 200 mb, and H_c between 0.1 and 1.0 (Diner *et al.*, 1982). Our nominal case is $H_c = 0.4$ and $p_c = 100$ mb.

Since these uncertainties affect the fit between our

TABLE 7. Imaginary part of the semidiurnal surface pressure oscillation.

Heating distribution	$\mathrm{Im}(p_s')_2$ (mb)
δ-function at ground	1.6
Diffusion model	0.3
Nominal model	−0.006
Step function at $\ln\sigma = -7$	0.03

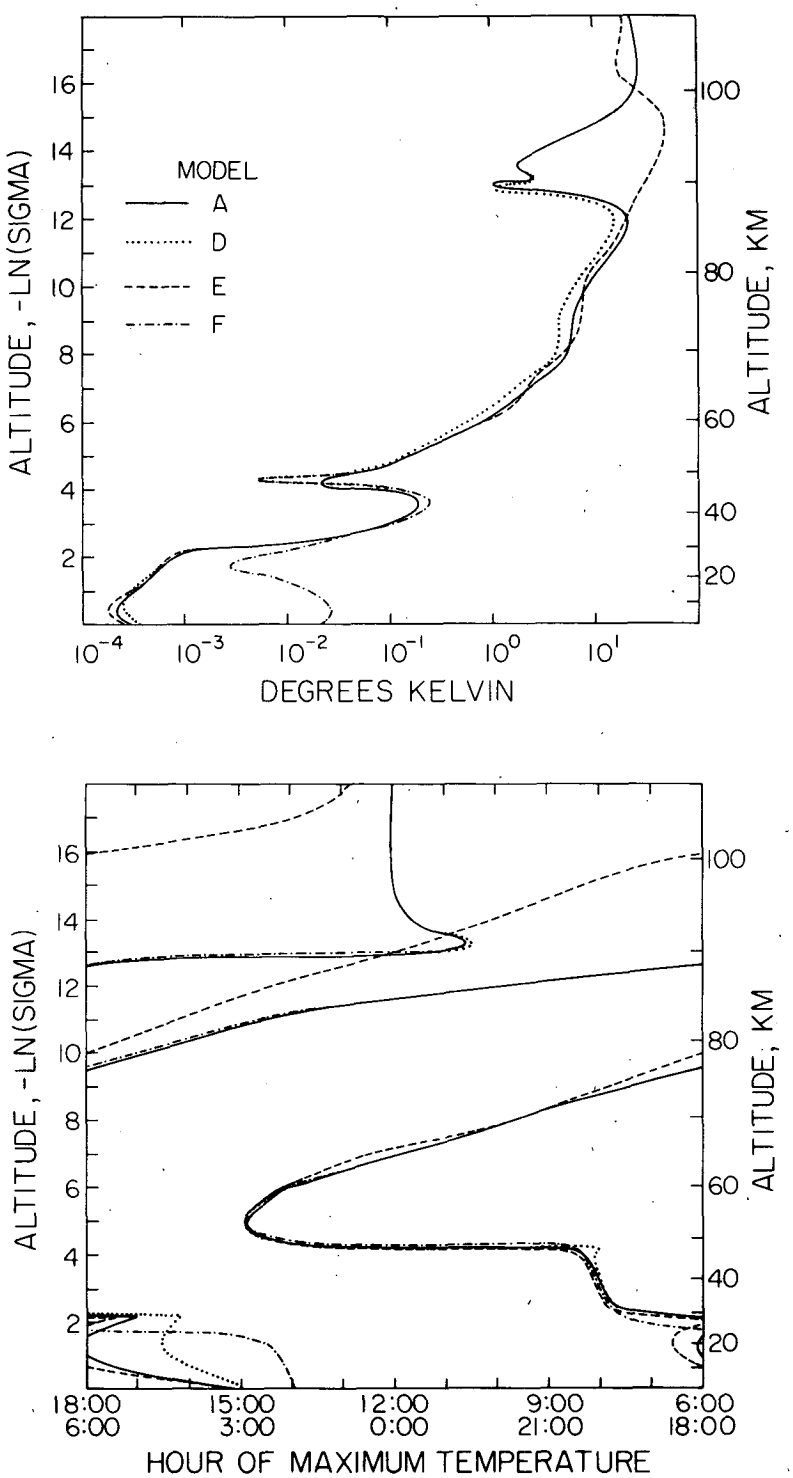

FIG. 22. Semidiurnal temperature oscillation at the equator using the gravity wave model. The solid curve is for the nominal model A. The dotted curve is for model D, whose zonal velocity profile is shown in Fig. 4. The dashed curve is for model E, whose zonal velocity profile is also shown in Fig. 4. The dot-dash curve is for model F, whose static stability profile is shown in Fig. 3. In other respects, models D, E and F have the same input parameters as model A.

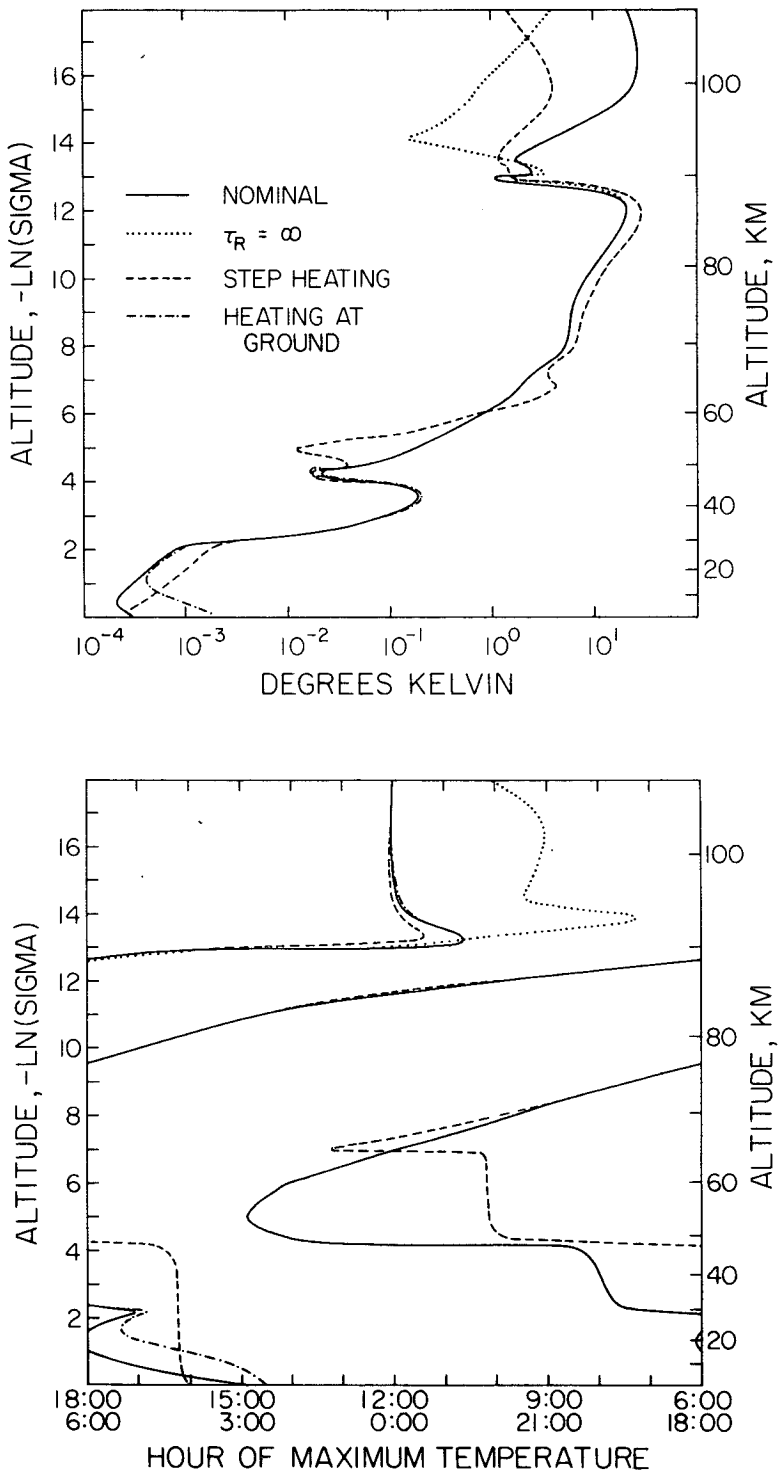

FIG. 23. Semidiurnal temperature oscillation at the equator using the gravity wave model. The solid curve is for the nominal model A. The dotted curve is the same as model A but with the time constant for Rayleigh friction set to infinity. The dashed curve is for a step function heating distribution, with a constant heating rate $dF/d\ln\sigma$ above $\ln\sigma = -7$ and 125 W m^{-2} absorbed on a global average. The basic state parameters are the same as model A. The dot-dash curve differs from model A in that it has an additional heating at the ground equivalent to globally averaged solar flux of 17 W m^{-2} absorbed in the lowest atmospheric layer.

TABLE 8. Sensitivity to cloud parameters: Semidiurnal tide at the equator.

		Channel 4		Channel 5	
H_c	p_c (mb)	Amplitude (deg)	Phase (h_{max})	Amplitude (deg)	Phase (h_{max})
0.4	50	4.3	0826	4.9	0829
0.4*	100*	3.1	0916	3.3	1000
0.4	200	2.5	0929	1.8	1112
0.4	300	2.3	0935	1.0	1111
0.85	100	2.9	0834	2.6	0843
0.85	200	2.6	0906	1.6	0953
0.15	50	4.4	0855	5.2	0915
0.15	100	2.8	0935	3.0	1055
OIR data		2.5	0900	2.6	1000

* Nominal model.

tidal model and the OIR data, we present Table 8 which shows the effects of varying H_c and p_c for the semidiurnal tide. As expected, channel 5 is more sensitive to changes in cloud parameters than channel 4 since it is a "window" channel designed to measure cloud top temperature. In the first four entries in Table 8 we hold H_c constant while p_c is varied. The phase in channel 5 at the equator was the determining factor in choosing p_c = 100 mb from this sequence. The agreement with the OIR data for p_c = 200 mb and H_c = 0.85 is as good as the nominal case. There is no unique best fit for H_c and p_c. We chose H_c = 0.4 for the nominal case because it is an intermediate value.

The diurnal results in channels 4 and 5 show a dependence on the cloud parameters similar to the semidiurnal results. However, the diurnal phase is more sensitive to change in the weighting functions because of its more rapid change with height.

The weighting functions used to calculate Tables 1–4, 6 and 8 assumed a viewing angle from the nadir of 35°. The OIR data used in the determination of the tides covered the range 0–69.5° (Taylor *et al.* 1980); we chose 35° as a representative value for the model. Changing the viewing angle to 0° has a negligible effect on the model brightness temperatures (Pechmann, 1983).

In summary, both the amplitudes and phases of the semidiurnal and diurnal brightness temperature oscillations as functions of latitude are adequately reproduced in our nominal tidal model. Convolving the model temperature structure with the OIR weighting functions is essential in computing model brightness temperatures, when these are to be compared with the OIR observations. Although we have not varied parameters of the basic state and tidal forcing exhaustively, our sensitivity studies indicate that the parameter values in our nominal case are at least close to the true values for Venus.

Acknowledgments. We thank Andrew N. Staniforth for sending the program of his primitive equation model, Arthur Raefsky for adapting it to the LPE, Lee S. Elson for providing OIR data and weighting functions, and David Crisp for providing his estimate of the radiative time constant. This research was supported by the Planetary Atmospheres Program of NASA under Grant NAGW-58.

REFERENCES

Betz, A. L., M. A. Johnson, R. A. McLaren and E. C. Sutton, 1976: Heterodyne detection of CO_2 emission lines and wind velocities in the atmosphere of Venus. *Astrophys. J.*, **208,** L141–L144.

——, E. C. Sutton, R. A. McLaren and C. W. McClary, 1977: Laser heterodyne spectroscopy. *Proc. Symp. on Planetary Atmospheres,* A. V. Jones, Ed., Royal Soc. Canada, Ottawa, 29–33.

Chapman, S., and R. S. Lindzen, 1970: *Atmospheric Tides: Thermal and Gravitational,* Gordon and Breach, 200 pp.

Counselman, C. C., III, S. A. Gourevitch, R. W. King and G. B. Loriot, 1980: Zonal and meridional circulation of the lower atmosphere of Venus determined by radio interferometry. *J. Geophys. Res.*, **85,** 8026–8030.

Dickinson, R. E., 1972: Infrared radiative heating and cooling in the Venusian mesosphere. I: Global mean radiative equilibrium. *J. Atmos. Sci.*, **29,** 1531–1556.

Diner, D. J., J. Apt and L. S. Elson, 1982: Comparison of ground-based and spacecraft observations of the infrared emission from Venus: The nature of thermal contrasts. *Icarus,* **52,** 301–319.

Dobrovolskis, A. R., and A. P. Ingersoll, 1980: Atmospheric tides and the rotation of Venus. I. Tidal theory and the balance of torques. *Icarus,* **41,** 1–17.

Elson, L. S., 1983: Solar related waves in the Venusian atmosphere from the cloud tops to 100 km. *J. Atmos. Sci.*, **40,** 1535–1551.

Gold, T., and S. Soter, 1969: Atmospheric tides and the resonant rotation of Venus. *Icarus,* **11,** 356–366.

——, and ——, 1971: Atmospheric tides and the 4-day circulation on Venus. *Icarus,* **14,** 16–20.

——, and ——, 1979: Theory of the Earth-synchronous rotation of Venus. *Nature,* **277,** 280–281.

Holton, J. R., 1979: *An Introduction to Dynamic Meteorology,* 2nd ed. Academic Press, 391 pp.

Ingersoll, A. P., and A. R. Dobrovolskis, 1978: Venus' rotation and atmospheric thermal tides. *Nature,* **275,** 37–38.

Kirkwood, E., and J. Derome, 1977: Some effects of the upper boundary condition and vertical resolution on modeling forced stationary planetary waves. *Mon. Wea. Rev.*, **105,** 1239–1251.

Kliore, A. J., and I. R. Patel, 1980: Vertical structure of the atmosphere of Venus from Pioneer Venus orbiter radio occultations. *J. Geophys. Res.*, **85,** 7957–7962.

——, and ——, 1982: Thermal structure of the atmosphere of Venus from Pioneer Venus radio occultations. *Icarus,* **52,** 320–334.

Limaye, S. S., and V. E. Suomi, 1981: Cloud motions on Venus: Global structure and organization. *J. Atmos. Sci.*, **38,** 1220–1235.

Lindzen, R. S., 1967: Thermally driven diurnal tide in the atmosphere. *Quart. J. Roy. Meteor. Soc.*, **93,** 18–42.

——, 1970: The application and applicability of terrestrial atmospheric tidal theory to Venus and Mars. *J. Atmos. Sci.*, **27,** 536–549.

——, 1971: Mathematical problems in the geophysical sciences. *Lectures in Applied Mathematics,* Vol. 14, Amer. Math. Soc., 293–360.

——, and H. Teitelbaum, 1984: Venus zonal wind above the cloud layer. *Icarus,* **57,** 356–361.

——, E. S. Batten and J. W. Kim, 1968: Oscillations in atmospheres with tops. *Mon. Wea. Rev.,* **96,** 133–140.

Pechmann, J., 1983: Thermal tides in the atmosphere of Venus. Ph.D. thesis, California Institute of Technology, 286 pp.

Pollack, J. B., and R. E. Young, 1975: Calculations of the radiative and dynamical state of the Venus atmosphere. *J. Atmos. Sci.,* **32,** 1025–1037.

——, O. B. Toon and R. Boese, 1980: Greenhouse models of Venus' high surface temperature, as constrained by Pioneer Venus measurements. *J. Geophys. Res.,* **85,** 8223–8231.

Robert, A., J. Henderson and C. Turnbull, 1972: An implicit time integration scheme for baroclinic models of the atmosphere. *Mon. Wea. Rev.,* **100,** 329–335.

Rossow, W. B., and E. Kinsella, 1982: Variations of winds on Venus. *Bull. Amer. Astron. Soc.,* **14,** 740.

——, A. D. Del Genio, S. S. Limaye and L. D. Travis, 1980: Cloud morphology and motions from Pioneer Venus images. *J. Geophys. Res.,* **85,** 8107–8128.

Schofield, J. T., and F. W. Taylor, 1983: Measurements of the mean, solar-fixed temperature and cloud structure in the middle atmosphere of Venus. *Quart. J. Roy. Meteor. Soc.,* **109,** 57–80.

Schubert, G., C. Covey, A. Del Genio, L. S. Elson, G. Keating, A. Seiff, R. E. Young, J. Apt, C. C. Counselman III, A. J. Kliore, S. S. Limaye, H. E. Revercomb, L. A. Sromovsky, V. E. Suomi, F. Taylor, R. Woo and U. von Zahn, 1980: Structure and circulation of the Venus atmosphere. *J. Geophys. Res.,* **85,** 8007–8025.

Seiff, A., D. B. Kirk, R. E. Young, R. C. Blanchard, J. T. Findlay, G. M. Kelly and S. C. Sommer, 1980: Measurements of thermal structure and thermal contrasts in the atmosphere of Venus and related dynamical observations: Results from the four Pioneer Venus probes. *J. Geophys. Res.,* **85,** 7903–7933.

Staniforth, A. N., and R. W. Daley, 1977: A finite-element formulation for the vertical discretization of sigma-coordinate primitive equation models. *Mon. Wea. Rev.,* **105,** 1108–1118.

Stone, P. H., 1974: The structure and circulation of the deep Venus atmosphere. *J. Atmos. Sci.,* **31,** 1681–1690.

Taylor, F. W., and collaborators, 1980: Structure and meteorology of the middle atmosphere of Venus: Infrared remote sensing from the Pioneer orbiter. *J. Geophys. Res.,* **85,** 7963–8006.

——, D. M. Hunten and L. V. Ksanfomaliti, 1983: The thermal balance of the middle and upper atmosphere of Venus. *Venus,* D. M. Hunten, L. Colin, T. M. Donohue and V. I. Moroz, Eds., University of Arizona Press, 650–680.

Tomasko, M. G., L. R. Doose, P. H. Smith and A. P. Odell, 1980a: Measurements of the flux of sunlight in the atmosphere of Venus. *J. Geophys. Res.,* **85,** 8167–8186.

——, P. H. Smith, V. E. Suomi, L. A. Sromovsky, H. E. Revercomb, F. W. Taylor, D. J. Martonchik, A. Seiff, R. Boese, J. B. Pollack, A. P. Ingersoll, G. Schubert and C. C. Covey, 1980b: The thermal balance of Venus in light of the Pioneer Venus mission. *J. Geophys. Res.,* **85,** 8187–8199.

Traub, W. A., and N. P. Carleton, 1975: Spectroscopic observations of winds on Venus. *J. Atmos. Sci.,* **32,** 1045–1059.

Woo, R., J. W. Armstrong and A. Ishimaru, 1980: Radio occultation measurements of turbulence in the Venus atmosphere by Pioneer Venus. *J. Geophys. Res.,* **85,** 8031–8038.